

Dieses Dokument ist eine Zweitveröffentlichung (Verlagsversion)

This is a self-archiving document (published version)

Marreddy Ambati, Jonas Heinzmann, Martha Seiler et al.

Phase-field modeling of brittle fracture along the thickness direction of plates and shells

Erstveröffentlichung in / First published in:

International journal for numerical methods in engineering. 2022. 123. Wiley. ISSN: 1097-0207.

DOI: <https://doi.org/10.1002/nme.7001>

Diese Version ist verfügbar / This version is available on:


<https://nbn-resolving.org/urn:nbn:de:bsz:14-qucosa2-882712>



Dieses Werk ist lizenziert unter einer [Creative Commons Namensnennung-Nicht kommerziell 4.0 International Lizenz](https://creativecommons.org/licenses/by-nc/4.0/).

This work is licensed under a [Creative Commons Attribution-NonCommercial 4.0 International License](https://creativecommons.org/licenses/by-nc/4.0/).

Phase-field modeling of brittle fracture along the thickness direction of plates and shells

Marreddy Ambati¹ | Jonas Heinzmann¹ | Martha Seiler¹ | Markus Kästner^{1,2,3} 

¹Institute of Solid Mechanics, Technische Universität Dresden, Dresden, Germany

²Dresden Center for Computational Materials Science, Technische Universität Dresden, Dresden, Germany

³Dresden Center for Fatigue and Reliability, Dresden, Germany

Correspondence

Markus Kästner, Institute of Solid Mechanics, Technische Universität Dresden, George-Bähr-Straße 3c, 01062 Dresden, Germany.
Email: markus.kaestner@tu-dresden.de

Funding information

Deutsche Forschungsgemeinschaft, Grant/Award Number: KA 3309/12-1

Abstract

The prediction of fracture in thin-walled structures is decisive for a wide range of applications. Modeling methods such as the phase-field method usually consider cracks to be constant over the thickness which, especially in load cases involving bending, is an imperfect approximation. In this contribution, fracture phenomena along the thickness direction of structural elements (plates or shells) are addressed with a phase-field modeling approach. For this purpose, a new, so called “mixed-dimensional” model is introduced, which combines structural elements representing the displacement field in the two-dimensional shell midsurface with continuum elements describing a crack phase-field in the three-dimensional solid space. The proposed model uses two separate finite element discretizations, where the transfer of variables between the coupled two- and three-dimensional fields is performed at the integration points which in turn need to have corresponding geometric locations. The governing equations of the proposed mixed-dimensional model are deduced in a consistent manner from a total energy functional with them also being compared to existing standard models. The resulting model has the advantage of a reduced computational effort due to the structural elements while still being able to accurately model arbitrary through-thickness crack evolutions as well as partly along the thickness broken shells due to the continuum elements. Amongst others, the higher accuracy as well as the numerical efficiency of the proposed model are tested and validated by comparing simulation results of the new model to those obtained by standard models using numerous representative examples.

KEYWORDS

fracture along thickness direction of shells, Kirchhoff–Love shell, mixed-dimensional model, partly through thickness broken shells, phase-field model

1 | INTRODUCTION

In the fields of mechanical, marine, aerospace, and civil engineering—especially in the context of lightweight structures—shells are considered as pivotal construction element. With the demand for increasing efficiency to for example, reduce the environmental impact, the common objective is to design such structures at their failure limit. This

This is an open access article under the terms of the Creative Commons Attribution-NonCommercial License, which permits use, distribution and reproduction in any medium, provided the original work is properly cited and is not used for commercial purposes.

© 2022 The Authors. *International Journal for Numerical Methods in Engineering* published by John Wiley & Sons Ltd.

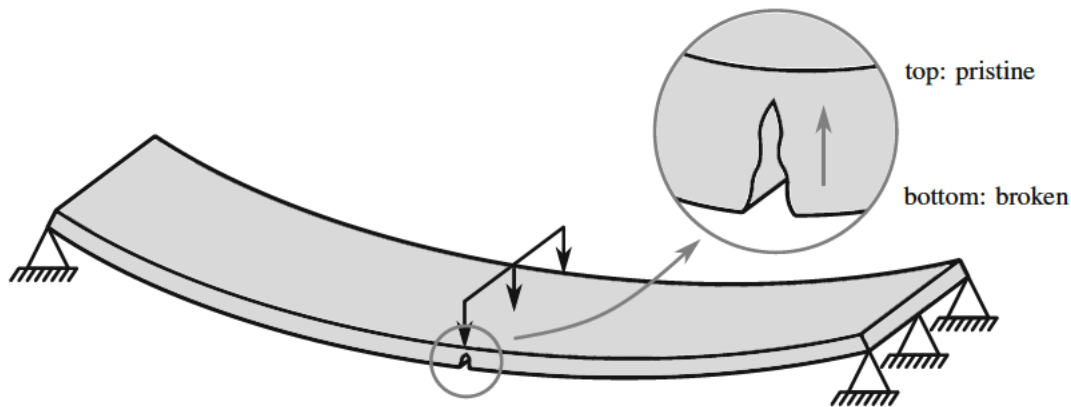


FIGURE 1 Crack initiation and evolution along the thickness direction in a bent plate (deformation exaggerated)

brings forth the need for mechanical models to predict fracture in thin walled structures. A particularly challenging task in modeling such structures is the correct consideration of the crack behavior along the thickness direction of a shell. This becomes evident even for an ordinary, moderately thin plate subjected to bending, such as the one shown in Figure 1. A crack initiates at the bottom of the plate—where the maximum tensile stress predominates—and evolves towards the top of the plate afterwards, see magnification in Figure 1. This phenomenon of cracks evolving along the thickness direction and partly through the thickness ranging cracks are of great theoretical and practical interest for shells and plates, see for instance Reference 1.

Although there are different approaches to model fracture in thin-walled structures, such as the extended finite element method (XFEM) introduced by Moës et al.² and applied to shells for instance in References 3-6 or meshfree methods, as applied to shells in References 7-9, especially the phase-field method has been the subject of extensive theoretical and computational investigations over the last two decades. Based on the energetic cracking criterion introduced by Griffith¹⁰ in 1921, the phase-field approach to brittle fracture is first formulated as a variational problem by Francfort and Marigo¹¹ in 1998 while the numerical implementation thereof was presented by Bourdin et al.¹² in 2000. The variational formulation within the mathematical theory of quasi-static brittle fracture mechanics revolves around the minimization problem of an energy functional recasting GRIFFITH'S theory into balancing the energy release rate during crack propagation with a fictitious surface energy. Motivated by the numerical implementation of this variational formulation, a phase-field (order) parameter is introduced to approximate the sharp crack discontinuity in a domain by a smooth transition between the fully broken and the fully intact material without the necessity for assuming any pre-defined cracks. A comprehensive overview of the existing phase-field fracture formulations considering monotonic loads is presented in Reference 13, see also the references therein. Due to its diffuse modeling approach which has the advantage that no remeshing at discontinuities is necessary, the phase-field approach to fracture has been applied to a broad range of problems such as fracture including inelastic deformations,^{14,15} viscoelastic materials,^{16,17} interface failure,^{18,19} heterogeneous materials,^{20,21} dynamic loading,^{22,23} fatigue failure,²⁴⁻²⁶ or fracture with anisotropy.^{27,28}

The phase-field approach to fracture has been applied to plates and shells in many different ways, focusing on various aspects. The first approach to couple a shell with the phase-field model for fracture was presented by Ulmer et al.²⁹ in 2012, where a shell is considered as combination of a KIRCHHOFF plate and a standard membrane. Amiri et al.⁷ in 2014 first coupled the phase-field approach to fracture with KIRCHHOFF-LOVE (KL) shell kinematics. An especially intriguing challenge for shells and plates comes with an anisotropic phase-field model, wherein only tensile terms are contributing to the crack evolution while compressive terms do not promote crack growth in order to approximate the real physical behavior more realistically.³⁰ For general phase-field continuum models, this is done by additively decomposing the elastic energy contribution into positive and negative parts for example, by spectral decomposition of the strain tensor as introduced by Miehe et al.³¹ While the first two aforementioned contributions for phase-field shell models do not consider this decomposition correctly with the first only splitting the membrane part and the second performing no split at all, Kiendl et al.³² in 2016 demonstrated for KL shells that a split of the complete strain tensor involving both membrane as well as bending action needs to be performed at various points over the shell thickness. Apart from various splits into tensile and compressive terms being presented, next to KL shell kinematics, the phase-field approach to

fracture has also been combined with higher-parametric shell models such as the REISSNER-MINDLIN (RM) shell theory, see for instance References 33,34. Further approaches to deal with the thinness of the structure in the context of phase-field modeling exist, such as a formulation with a mixed interpolation of tensorial components (MITC)4+ RM degenerated shell³⁵ and a solid-shell approach.^{36,37} Taken together, the phase-field approach to fracture applied to shells has been subject of extensive research in the recent years, focusing mainly on the extension to specific problems, namely ductile fracture,³⁸ finite strains,³⁹ functionally graded materials,⁴⁰ thick shells,⁴¹ dynamic problems^{42,43} as well as the isogeometric implementation with adaptive refinement⁴⁴ or multipatch coupling techniques.⁴⁵

However, the application of the phase-field approach to model cracks along the thickness direction of shells has been given very limited attention up until now. To the author's best knowledge, except two contributions,^{46,47} all of the aforementioned models consider the phase-field to be constant along the thickness direction of shells argued for with their slenderness. Thereby, these models are exclusively able to represent cracks which do not vary along the thickness direction. The first exception to this is a contribution by Areias et al.⁴⁶ where for finite-strain plates and shells, two independent phase-fields are considered at the very top and very bottom of the shell structure, as similarly motivated for XFEM in Reference 48. With these two degrees of freedom (DOFs) at the top and bottom of the shell, the model can differentiate between either the top or bottom being broken and a through-thickness crack when both of the independent phase-fields indicate broken material. However, no continuous crack evolution along the thickness direction can be described with this model. The second contribution posing an exception, presented by Lai et al.⁴⁷—although only considering EULER-BERNOULLI beams with the aim to generalize the approach to plate and shell problems—introduces a double sigmoid ansatz function to represent phase-field variation along the thickness direction in the otherwise one-dimensional structure. Thereby, the model is able to depict partly through the thickness ranging cracks, however restricted to the chosen ansatz without a variable length scale of the phase-field.

This is why the aim of this article is to propose a new phase-field approach for brittle fracture in shell structures which accurately describes arbitrary through-thickness crack evolutions as well as partly through the thickness broken shells. To do so, this new model combines

- **shell elements representing the displacement field**, which is thereby defined in a two-dimensional (2D) curvilinear coordinate system clinging to the structure and
- **solid elements representing the phase-field**, which is thereby defined in a three-dimensional (3D) curvilinear coordinate system.

According to the notion of combining elements of different dimensions for the fields of a coupled boundary value problem (BVP), the suggested model is termed as “mixed-dimensional model.” The shell element in this article is exemplarily based on KL shell kinematics in a rotation-free, non-uniform-rational-basis-spline (NURBS)-based isogeometric formulation⁴⁹ which is well investigated in literature with respect to many regards such as for example, finite strains,^{50,51} inelastic deformations,^{52,53} or coupling of multiple patches.⁵⁴⁻⁵⁷ Regardless of this exemplary chosen shell theory, other, higher-parametric shell kinematics would be feasible for the proposed mixed-dimensional model as well, see for instance Reference 58 for isogeometric formulations of various shell models. By coupling this shell model to a fully 3D phase-field description, the reduced computational effort of a structural element is preserved while refraining from any assumptions or simplifications in the phase-field. Although the idea of combining solid and structural elements to describe various parts of a structure, such as done for instance in References 59-63, or even different parts within each other for reinforced structures as for example, in References 64-66 is not new, the idea to combine solid and structural elements for different fields of a coupled BVP has not been presented before.

The article is outlined as follows: in Section 2, after introducing the preliminary geometry definitions and the kinematics, a total energy functional for the coupled field problem of a 3D solid model and a previous shell model, which is fully defined in the 2D shell midsurface by introducing a constant phase-field over the thickness is presented. Using this as a starting point, the governing equations of the proposed mixed-dimensional model are derived. As all of these models are deduced from the same total energy functional, special attention is paid to their similarities and differences in a comparison throughout. Implementation aspects of the proposed model including algorithmic and solution aspects are outlined in Section 3. In Section 4, the results of several benchmark examples obtained by the proposed model are presented and compared with the standard solid and shell model results to confirm the accuracy and improvement. Finally, Section 5 gives an summary and outlook on future work.

2 | FORMULATION

This section is devoted to the detailed presentation of the proposed mixed-dimensional model. Beforehand, the required geometric and kinematic quantities are briefly reviewed. Afterwards, the standard phase-field model for three-dimensional solids is presented first as a starting point and for comparison purposes. For the same reasons, the previous fracture model for shells is provided subsequently. Finally, the proposed mixed-dimensional phase-field fracture formulation of plates and shells is derived. All formulations are limited to linear elasticity as well as small displacements and rotations in this article.

2.1 | Kinematics

For the general description in 3D EUCLIDIAN space \mathbb{R}^3 , a curvilinear coordinate system clinging to the structure with the coordinates $\Theta^i = \{\Theta^1, \Theta^2, \Theta^3\}$ is considered. Necessary for the subsequently presented models, two different geometric spaces are introduced as illustrated in Figure 2:

- First, the 3D solid space $V \in \mathbb{R}^3$ is introduced. For a description of a point belonging to this solid space, all three coordinates $(\Theta^1, \Theta^2, \Theta^3)$ are needed. The third coordinate Θ^3 describes the thickness direction of the structure, while the coordinate system is defined such that $\Theta^3 = 0$ is always exactly in the middle of the thickness t of the structure, that is, $\Theta^3 \in [-t/2, +t/2]$. In the solid space, the position vector of any material point of the undeformed structure is given by $\mathbf{X} = X\mathbf{e}_x + Y\mathbf{e}_y + Z\mathbf{e}_z$ with respect to the global CARTESIAN basis system.
- Second, the 2D shell midsurface $A \subset V$ is introduced. It is constituted by all points of the solid space with $\Theta^3 = 0$ such that $\mathbf{R} = \{\mathbf{X} \in V \mid \Theta^3 = 0\} \in A$ holds for the position vector of any given material point of the undeformed shell midsurface with respect to the global CARTESIAN basis system.

It is important to emphasize that both—the solid space and shell midsurface—share the coordinate pair (Θ^1, Θ^2) , with the 2D coordinate system of the shell midsurface missing the thickness coordinate Θ^3 . For a clear notation in this article and to distinguish between both geometric spaces, Latin indices $(i, j, k, \dots) = (1, 2, 3)$ are used to refer the coordinate tuple Θ^i for the solid space V , while Greek indices $(\alpha, \beta, \gamma, \dots) = (1, 2)$ are adopted to denote the coordinate pair Θ^α for the shell midsurface A . Furthermore, superscripts $(\cdot)^i$ refer to contravariant components of a vector while subscripts $(\cdot)_i$ refer to covariant components. Following this, spatial derivatives in the solid space with respect to Θ^i are abbreviated by $(\cdot)_{,i} = \partial(\cdot)/\partial\Theta^i$ while $(\cdot)_{,\alpha} = \partial(\cdot)/\partial\Theta^\alpha$ indicates the spatial derivatives in the shell midsurface with respect to Θ^α . Index notation and EINSTEIN'S summation convention are adopted in this manner, except for upright sub- and superscripts which instead are used to distinguish i.a. between the displacement field $(\cdot)_u$ and the phase-field $(\cdot)_c$.

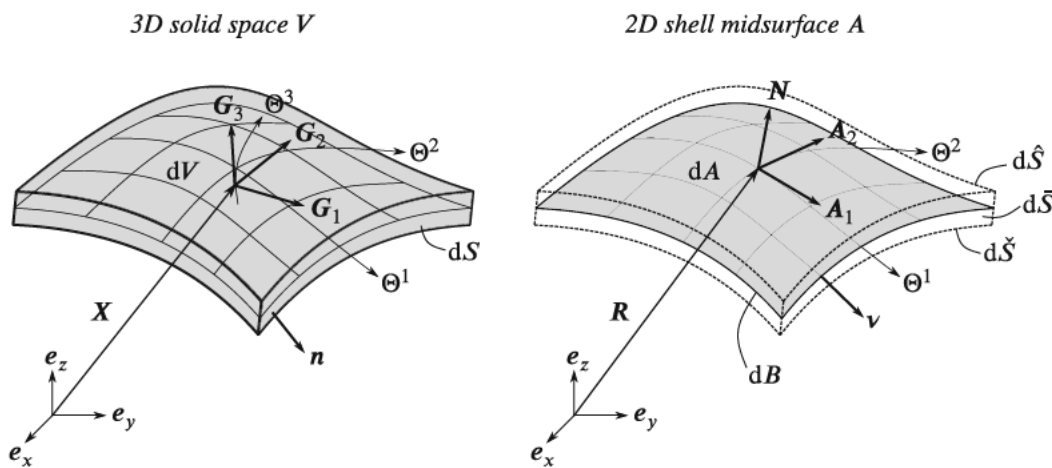


FIGURE 2 Geometric definitions of the three-dimensional solid space and the two-dimensional shell midsurface

Starting with the geometry and kinematics for 3D solids, the covariant basis vectors \mathbf{G}_i of the initial, undeformed 3D solid space V are given by

$$\mathbf{G}_i(\Theta^i) = \frac{\partial \mathbf{X}(\Theta^1, \Theta^2, \Theta^3)}{\partial \Theta^i} = \mathbf{X}_{,i}, \quad (1)$$

while the covariant components of the metric tensor G_{ij} are computed as

$$G_{ij} = \mathbf{G}_i \cdot \mathbf{G}_j. \quad (2)$$

With the mere restriction being small displacements and small deformations, the components of the geometrically linearized strain tensor ε_{kl} for a general 3D solid are given by

$$\varepsilon_{kl} = \frac{1}{2} (u_{k|l} + u_{l|k}), \quad (3)$$

where \mathbf{u} is the displacement vector and $(\cdot)_{k|l}$ denotes the covariant derivative in curvilinear coordinate systems.

Moving on to the 2D shell midsurface A with the position vector $\mathbf{R}(\Theta^\alpha)$, the covariant base vectors \mathbf{A}_α therein are obtained as

$$\mathbf{A}_\alpha(\Theta^\alpha) = \frac{\partial \mathbf{R}(\Theta^1, \Theta^2)}{\partial \Theta^\alpha} = \mathbf{R}_{,\alpha}. \quad (4)$$

The normal base vector perpendicular to the shell midsurface is computed by

$$\mathbf{N} = \frac{\mathbf{A}_1 \times \mathbf{A}_2}{\|\mathbf{A}_1 \times \mathbf{A}_2\|} \quad (5)$$

with $\mathbf{A}_\alpha \cdot \mathbf{N} = 0$. With these base vectors being defined, the first and second fundamental form of the shell midsurface are then obtained as

$$A_{\alpha\beta} = \mathbf{A}_\alpha \cdot \mathbf{A}_\beta, \quad (6a)$$

$$B_{\alpha\beta} = \mathbf{A}_{\alpha,\beta} \cdot \mathbf{N}, \quad (6b)$$

where $A_{\alpha\beta}$ represent the covariant components of the metric tensor and $B_{\alpha\beta}$ denote the components of the curvature tensor of the shell midsurface. Furthermore, the mixed variant components of the curvature tensor are calculated as $B^\alpha_\beta = A^{\alpha\gamma} B_{\gamma\beta}$.

As already mentioned in the introduction, the KL shell theory is adopted in this work for the definition of the shell kinematics. On the prerequisite that the shell thickness t is comparably small and the main curvature radii ρ_α is comparably large in relation to the lateral dimensions of the shell, the KL theory postulates that cross lines initially perpendicular to the shell midsurface remain straight and perpendicular during deformation (normal hypothesis), resulting in vanishing components of the strain tensor in the thickness direction, that is, $\varepsilon_{\alpha 3} = \varepsilon_{3\alpha} \equiv 0$. Furthermore, any changes of the shell thickness t are neglected which means that the initial geometry has a constant thickness ($t_{,\alpha} \equiv 0$) and that the deformation has no influence on the thickness direction ($\varepsilon_{33} \equiv 0$). With these assumptions, in a geometrically linearized setting, the strain tensor of the shell midsurface is given by

$$\varepsilon_{\lambda\mu} = \frac{1}{2} (u_{\lambda|\mu} + u_{\mu|\lambda}), \quad (7)$$

which can be rewritten as

$$\varepsilon_{\lambda\mu} \approx \frac{1}{2} (\mathbf{u}_{,\lambda} \cdot \mathbf{A}_\mu + \mathbf{u}_{,\mu} \cdot \mathbf{A}_\lambda). \quad (8)$$

These KL kinematics feature an ansatz for the displacement which is distributed linearly along the thickness direction Θ^3

$$u_k(\Theta^\alpha, \Theta^3) = u_k^0(\Theta^\alpha) + \Theta^3 u_k^1(\Theta^\alpha), \quad (9)$$

comprising a constant part $\overset{0}{\mathbf{u}}$ and a linear part $\overset{1}{\mathbf{u}}$. Substituting for example, (9) into (8) yields with further kinematic quantities the final strain components $\epsilon_{\alpha\beta}$ of the shell midsurface

$$\epsilon_{\alpha\beta} = \eta_{\alpha\beta} + \Theta^3 \kappa_{\alpha\beta}, \tag{10}$$

which entails the constant membrane action $\boldsymbol{\eta}$ along the thickness direction and the linear bending action $\boldsymbol{\kappa}$ along the thickness direction.

2.2 | Standard three-dimensional phase-field fracture formulation of solids

Now, the derivation of standard phase-field brittle fracture model, which acts as part of the basis and as benchmark for the proposed model later on, is presented first. Following the formulation introduced in Reference 67, the standard phase-field model is based on the minimization problem of the total energy functional \mathcal{E} given by

$$\mathcal{E}(\epsilon_{kl}, \Gamma) = \int_V \Psi_u(\epsilon_{kl}) dV + \int_{\Gamma} \mathcal{G}_c d\Gamma, \tag{11}$$

where Ψ_u is the elastic strain energy density, \mathcal{G}_c is the material specific fracture toughness and Γ is the set of crack surfaces inside V . Using the smeared crack approach of the phase-field method,^{31,67} the fracture energy density Ψ_c —originally computed with the integral of \mathcal{G}_c over the crack surface Γ —can be regularized as

$$\int_{\Gamma} \mathcal{G}_c d\Gamma \approx \int_V \Psi_c(c, c_n) dV = \int_V \mathcal{G}_c \left[\frac{1}{4l} (1 - c)^2 + lc_n c_n \right] dV, \tag{12}$$

where $c \in [0, 1]$ is the phase-field variable with $c = 1$ representing fully intact material and $c = 0$ representing fully cracked material. This scalar field variable distributes the crack over a finite length which is proportional to the internal length scale l . To couple the phase-field variable to the displacement field, the elastic energy density is degraded with the degradation function $g(c) = (1 - g_0)c^2 + g_0$ featuring the residual stiffness g_0 to avoid numerical difficulties. Moreover, to differentiate between the fracture behavior for tensional and compressional loading, the elastic strain energy density Ψ_u is decomposed into a tensile Ψ_u^+ and a compressive contribution Ψ_u^- while only the positive part is degraded. Such an additive decomposition can be made based on strains or stress, several strategies exist for this purpose.^{31,68,69} The final regularized form of the functional is given by

$$\mathcal{E} = \int_V g(c) \Psi_u^+(\epsilon_{kl}) + \Psi_u^-(\epsilon_{kl}) + \Psi_c(c, c_n) dV. \tag{13}$$

The governing equations of the problem are obtained by minimizing this free energy functional using variational principles. According to these, the first variation of the free energy functional (13) with respect to the phase-field variable $\delta\mathcal{E}_c$ results in the phase-field evolution equation

$$\delta\mathcal{E}_c = \int_V \left(\frac{\partial g}{\partial c} \Psi_u^+ + \frac{\partial \Psi_c}{\partial c} \right) \delta c + \left(\frac{\partial \Psi_c}{\partial c_n} \right) \delta c_n dV. \tag{14}$$

Using integration by parts and applying GAUSS' theorem with the normal vector \mathbf{n} on the boundary S , (14) can be rewritten as

$$\delta\mathcal{E}_c = \int_V \left[2(1 - g_0)c \Psi_u^+ - \frac{\mathcal{G}_c}{2l} (1 - c) - (2\mathcal{G}_c lc_n)_{|n} \right] \delta c dV + \oint_{\partial V} n^m (2\mathcal{G}_c lc_m \delta c) dS. \tag{15}$$

Considering that the first variation must vanish for arbitrary δc , the strong form and the NEUMANN boundary condition of the standard 3D phase-field model ultimately read as

$$\left[\frac{4l(1-g_0)\mathcal{H}}{\mathcal{G}_c} + 1 \right] c - 4l^2 (c,n)_{|n} = 1 \quad \forall \mathbf{X} \in V, \quad (16a)$$

$$n^m c_{,m} = 0 \quad \forall \mathbf{X} \in \partial V. \quad (16b)$$

Herein, a damage-like irreversibility constraint is incorporated to ensure that the phase-field variable only grows larger using a local history variable \mathcal{H} defined as

$$\mathcal{H}(t) = \max_{\tau < t} [\Psi_u^+(\tau)]. \quad (17)$$

Likewise, requiring a geometrically linear setting and exploiting GAUSS' theorem, the first variation of (13) with respect to the displacement $\delta \mathcal{E}_u$ results in the strong form and the NEUMANN boundary condition of the displacement field

$$\sigma^{kl}{}_{|l} + \rho f^k = 0 \quad \forall \mathbf{X} \in V, \quad (18a)$$

$$\sigma^{kl} n_k = t^l \quad \forall \mathbf{X} \in \partial V \quad (18b)$$

with σ representing CAUCHY's stress tensor

$$\sigma^{kl} = g(c) \frac{\partial \Psi_u^+}{\partial \varepsilon_{kl}} + \frac{\partial \Psi_u^-}{\partial \varepsilon_{kl}} = g(c) \sigma^{+kl} + \sigma^{-kl}. \quad (19)$$

In (18), \mathbf{f} is the vector of body forces acting in V which is of density ρ and \mathbf{t} is the surface traction vector acting on the boundary S . For brevity, the model defined by (16) and (18)—both fully referring to the 3D space—is called “solid model” in the following.

2.3 | Previous two-dimensional phase-field fracture formulation of plates and shells

To adapt the solid model previously presented in Section 2.2 to plates and shells, various concepts exist.^{7,29,32,34} In this article, the seminal model presented in Reference 32 is adopted. To do so, the functional given in (13) is modified to

$$\mathcal{E} = \int_A g(c) \Psi_t^+(\varepsilon_{\alpha\beta}) + \Psi_t^-(\varepsilon_{\alpha\beta}) + t \Psi_c(c, c_{,\alpha}) \, dA, \quad (20)$$

wherein Ψ_t denotes the strain energy surface density. This modification of the energy functional is based on the reduction of the 3D solid space V to the 2D shell midsurface A by integrating over the thickness t of the thin-walled structure. Naturally, the chosen shell kinematics play the key role in this for the displacement field; for the phase-field however, the adopted model is based on the postulation that the phase-field variable is constant over the thickness such that it only depends on the position on the shell midsurface $c = c(\Theta^\alpha)$; that is, $c \neq c(\Theta^3)$ which is argued for by the slenderness of plates and shells. Such a non-existent dependence of c on the thickness coordinate Θ^3 allows to pre-integrate (12) analytically

$$\int_V \mathcal{G}_c \left[\frac{1}{4l}(1-c)^2 + lc_{,n}c_{,n} \right] \, dV = \int_A \int_t \mathcal{G}_c \left[\frac{1}{4l}(1-c)^2 + lc_{,n}c_{,n} \right] \, d\Theta^3 \, dA \stackrel{c \neq c(\Theta^3)}{=} t \int_A \mathcal{G}_c \left[\frac{1}{4l}(1-c)^2 + lc_{,\alpha}c_{,\alpha} \right] \, dA. \quad (21)$$

Furthermore, as pointed out in Reference 32, the way to perform the split into tensile and compressive elastic energy contributions poses another challenge due to the definition of the strain tensor (10) for plates and shells: to model the material response for tension and compression correctly, the spectral decomposition of the strain tensor as a whole is necessary

$$\varepsilon_{\alpha\beta}^\pm = (\eta_{\alpha\beta} + \Theta^3 \kappa_{\alpha\beta})^\pm = \sum_{\lambda=1}^3 \langle \varepsilon_\lambda \rangle^\pm \mathbf{n}_\lambda \otimes \mathbf{n}_\lambda \neq \eta_{\alpha\beta}^\pm + \Theta^3 \kappa_{\alpha\beta}^\pm, \quad (22)$$

where ε_λ are the eigenvalues, \mathbf{n}_λ are the eigenvectors and $\langle \cdot \rangle^\pm = (\cdot \pm |\cdot|)/2$ holds. Using (22), the earlier introduced strain energy density per unit area of the midsurface can finally be obtained as

$$\Psi_t^\pm = \int_t \Psi_u^\pm(\Theta^3) d\Theta^3 \tag{23}$$

with Ψ_u referring back to the strain energy density at arbitrary points in the 3D solid space. As shown in Reference 32, such a split results in a non-linear distribution of $\sigma_{\alpha\beta}$ and Ψ_t^\pm over the shell thickness, which is why the displacement parts in the energy functional cannot be integrated over the thickness analytically anymore. Instead, numerical integration is necessary. Finally, the first variation of the energy functional adopted to shells with respect to the phase-field variable—in comparison to (14)—leads to

$$\delta \mathcal{E}_c \stackrel{c=c(\Theta^\alpha)}{=} \int_A \left(\frac{\partial g}{\partial c} \Psi_t^+ + t \frac{\partial \Psi_c}{\partial c} \right) \delta c + \left(t \frac{\partial \Psi_c}{\partial c_{,\alpha}} \right) \delta c_{,\alpha} dA. \tag{24}$$

Ultimately, the strong form and the NEUMANN boundary condition of the phase-field then read as

$$\left[\frac{4l(1-g_0)\mathcal{H}_t}{t\mathcal{G}_c} + 1 \right] c - 4l^2 (c_{,\alpha})_{|\alpha} = 1 \quad \forall \mathbf{R} \in A, \tag{25a}$$

$$\mathbf{v}^\alpha c_{,\alpha} = 0 \quad \forall \mathbf{R} \in \partial A \tag{25b}$$

with \mathbf{v} as the normal vector on the boundary of the shell midsurface and the modified history variable $\mathcal{H}_t = \max_{\tau < t} [\Psi_t^+(\tau)]$ referring to the thickness-integrated strain energy density contribution.

For the displacement field of the previous phase-field model for shells, the first variation of the functional in (13) with respect to the displacement is

$$\delta \mathcal{E}_u = \int_A \int_t \sigma^{\alpha\beta} (\delta \eta_{\alpha\beta} + \Theta^3 \delta \kappa_{\alpha\beta}) d\Theta^3 dA, \tag{26}$$

while σ now is given by

$$\sigma^{\alpha\beta} = g(c) \frac{\partial \Psi_u^+}{\partial \varepsilon_{\alpha\beta}} + \frac{\partial \Psi_u^-}{\partial \varepsilon_{\alpha\beta}} = g(c) \sigma^{+\alpha\beta} + \sigma^{-\alpha\beta}. \tag{27}$$

With the introduction of membrane forces \mathbf{n} and bending moments \mathbf{m} as stress resultants

$$\mathbf{n}^{\alpha\beta} = \int_t (g(c) \sigma^{+\alpha\beta} + \sigma^{-\alpha\beta}) d\Theta^3 \quad \mathbf{m}^{\alpha\beta} = \int_t \Theta^3 (g(c) \sigma^{+\alpha\beta} + \sigma^{-\alpha\beta}) d\Theta^3, \tag{28}$$

the first variation of the modified energy functional (26) can be rewritten as

$$\delta \mathcal{E}_u^1 = \int_A \mathbf{n}^{\alpha\beta} \delta \eta_{\alpha\beta} + \mathbf{m}^{\alpha\beta} \delta \kappa_{\alpha\beta} dA. \tag{29}$$

Using this—omitting the detailed derivation for conciseness in this article—the strong form of the KL shell can eventually be determined as

$$-\mathbf{n}^{\gamma\delta}_{|\delta} + \mathbf{m}^{\alpha\beta} B^\gamma_{\alpha|\beta} + 2\mathbf{m}^{\alpha\beta}_{|\beta} B^\gamma_{\alpha} = p^\gamma - \omega^\beta B^\gamma_{\beta} \quad \forall \mathbf{R} \in A, \tag{30a}$$

$$-\mathbf{n}^{\alpha\beta} B_{\alpha\beta} + \mathbf{m}^{\alpha\beta} B^\gamma_{\alpha} B_{\beta\gamma} - \mathbf{m}^{\alpha\beta}_{|\beta\alpha} = p^3 + \omega^\alpha_{|\alpha} \quad \forall \mathbf{R} \in A, \tag{30b}$$

while the corresponding NEUMANN boundary conditions result from the boundary terms

$$\mathbf{n}^{\gamma\beta} \nu_\beta - 2\mathbf{m}^{\alpha\beta} B^\gamma_{\alpha} \nu_\beta = q^\gamma - \phi^\beta B^\gamma_{\beta} \quad \forall \mathbf{R} \in \partial A, \tag{31a}$$

$$\mathbf{m}^{\alpha\beta}_{|\beta} \nu_\alpha + \omega^\alpha \nu_\alpha = q^3 \quad \forall \mathbf{R} \in \partial A, \tag{31b}$$

$$\mathbf{m}^{\alpha\beta} \nu_\beta = \phi^\alpha \quad \forall \mathbf{R} \in \partial A, \tag{31c}$$

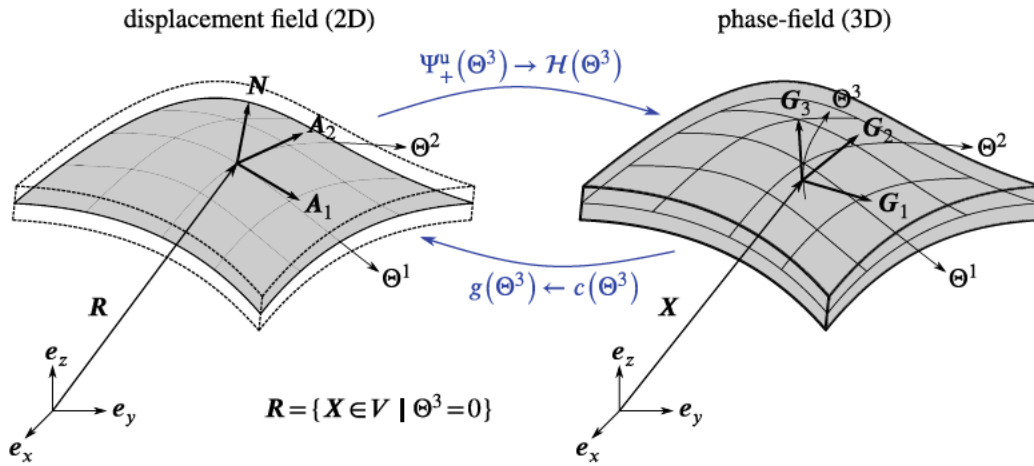


FIGURE 3 Basic idea of the new mixed-dimensional model

wherein \mathbf{p} is force per midsurface area, $\boldsymbol{\omega}$ is momentum per midsurface area, \mathbf{q} is the force per length of the midsurface boundary and $\boldsymbol{\phi}$ is the momentum per length of the midsurface boundary. For brevity, this model defined by (25), (30), and (31) is called “shell model” in the following. Note that in comparison to the strong form of the 3D displacement field (18a), the strong form of the shell model now refers to all points of the shell midsurface $\mathbf{R} \in A$ instead of the solid space $\mathbf{X} \in V$. Also, as mentioned beforehand, this phase-field approach to fracture in plates and shells is not able to describe non-constant behavior of the crack along their thickness direction since $c \neq c(\Theta^3)$, which inspires the underlying concept and the model presented in the next section.

2.4 | Proposed mixed-dimensional phase-field fracture formulation of plates and shells

To overcome this drawback while still exploiting the reduced computational effort of a shell model, the new model is proposed now. The key idea of this model is to combine a shell, that is, a midsurface representation of the displacement field with a 3D representation of the phase-field taken from a solid model, such as illustrated in Figure 3. It is called “mixed-dimensional” model in the following as both of the geometric spaces are a prerequisite of the model. Specifically, the 3D solid space V is considered for the phase-field representation, which means the phase-field variable is dependent on all three coordinates Θ^k , that is, $c = c(\Theta^\alpha, \Theta^3)$ whereas the 2D shell midsurface A is used for the displacement field representation.

The starting point once again is the energy functional (13), however in a slightly altered way, so that the basic idea of the mixed-dimensional model manifests itself in a consistent manner. The elastic strain energy contribution is integrated over the thickness to reduce the 3D field to the 2D shell midsurface while the phase-field part is still kept in its 3D form

$$\mathcal{E} = \underbrace{\int_A g(c) \Psi_t^+(\epsilon_{\alpha\beta}) + \Psi_t^-(\epsilon_{\alpha\beta}) \, dA}_{\text{from shell model}} + \underbrace{\int_V \Psi_c(c, c_n) \, dV}_{\text{from solid model}}. \quad (32)$$

This functional can thereby be understood as combination of the displacement field description of the shell model with the phase-field description of the solid model. From (32), the strong form of the displacement field is obtained analogously to the shell model as

$$-n^{\gamma\delta}{}_{|\delta} + m^{\alpha\beta} B^\gamma{}_{\alpha|\beta} + 2m^{\alpha\beta}{}_{|\beta} B^\gamma{}_{\alpha} = p^\gamma - \omega^\beta B^\gamma{}_{\beta} \quad \forall \mathbf{R} \in A, \quad (33a)$$

$$-n^{\alpha\beta} B_{\alpha\beta} + m^{\alpha\beta} B^\gamma{}_{\alpha} B_{\beta\gamma} - m^{\alpha\beta}{}_{|\beta\alpha} = p^3 + \omega^\alpha{}_{|\alpha} \quad \forall \mathbf{R} \in A, \quad (33b)$$

while the strong form of the phase-field—obtained in the same way as for the solid model—takes the form

$$\left[\frac{4l(1-g_0)\mathcal{H}}{\mathcal{G}_c} + 1 \right] c - 4l^2 (lc_n)_{|n} = 1 \quad \forall \mathbf{X} \in V. \quad (34)$$

The corresponding NEUMANN boundary conditions of the displacement field (31) and the phase-field (16b) apply for this case. Clearly, the strong forms of the mixed-dimensional model can also be identified as a combination of displacement part of the shell model (30) with the phase-field part of the solid model (16a). In order to couple both of these fields—now remarkably referring to different geometric entities—with each other, $\mathbf{R} = \{\mathbf{X} \in V \mid \Theta^3 = 0\}$ has to hold to enable the translation between each material point of the shell midsurface and the corresponding material point of the solid. Given (33) and (34), the following coupling quantities can be identified:

- The phase-field variable $c(\Theta^3)$ involved in the degradation function g is needed for the computation of the stress resultants when solving for the displacement field (33).
- The positive strain energy density contribution $\Psi_u^+(\Theta^3)$ is required as an energetic crack driving force that is, for updating the local history variable \mathcal{H} when solving for the phase-field (34).

Allowing the interchange of these coupling quantities between the two different geometric spaces in the first place is the circumstance that the underlying and substituted structure of the shell is still a 3D solid which is reduced to the shell midsurface by integrating over the thickness. This thickness integration in fact is exactly what enables the combination of 2D and 3D fields in the first place, since the strains and stresses are still dependent on the thickness coordinate. Consequently, this manifests itself in a slightly altered definition of the stress resultants

$$n^{\alpha\beta}(\Theta^\alpha) = \int_t \{g[c(\Theta^\alpha, \Theta^3)] \sigma^{+\alpha\beta} + \sigma^{-\alpha\beta}\} d\Theta^3, \tag{35a}$$

$$m^{\alpha\beta}(\Theta^\alpha) = \int_t \Theta^3 \{g[c(\Theta^\alpha, \Theta^3)] \sigma^{+\alpha\beta} + \sigma^{-\alpha\beta}\} d\Theta^3, \tag{35b}$$

due to the now thickness-dependent degradation function, whereas the strain energy per unit area of the midsurface $\Psi_u^\pm[\varepsilon_{\alpha\beta}(\Theta^3)]$ can be directly obtained at various points of the shell thickness.

In contrast to previous phase-field fracture models of plates and shells, the mixed-dimensional model is able to fully represent an arbitrary through-thickness behavior of the phase-field, which entails not only the phase-field variable c itself but also the gradient ∇c thereof, while still keeping the simplified shell model. Only exemplary, the KL shell theory is utilized in this article due to its suitability to isogeometric analysis (IGA), while it is important to note that other shell models with a higher count of parameters (e.g., RM shell kinematics) are equally feasible for the mixed-dimensional model as well.

3 | IMPLEMENTATIONAL ASPECTS

The coupling of shell elements to solid elements naturally raises the question of the actual finite element (FE) implementation. Thus, this section is devoted to give a brief overview of the most important implementational aspects regarding the mixed-dimensional model.

3.1 | Numerical solution scheme

The set of coupled partial differential equations given by the strong forms in (33) and (34) are solved using NURBS-based IGA since it allows a rotationless FE formulation.⁴⁹ For that purpose, the weak forms with appropriate test functions—here indicated by $\tilde{(\cdot)}$ —are introduced: the weak form of the phase-field evolution equation of the solid part is given by

$$\int_V \tilde{c} \left(\frac{4l(1-g_0)\mathcal{H}}{\mathcal{G}_c} + 1 \right) c dV + \int_V 4l^2 \nabla \tilde{c} \cdot \nabla c dV = \int_V \tilde{c} dV. \tag{36}$$

For the displacement field, the weak form of the shell part reads as

$$\int_A \mathbf{n} : \tilde{\boldsymbol{\eta}} + \mathbf{m} : \tilde{\boldsymbol{\kappa}} dA = \int_A \mathbf{r} \cdot \tilde{\mathbf{u}} dA \tag{37}$$

with all external forces being consolidated into the vector \mathbf{r} . A staggered solution scheme including convergence criteria is adopted to solve the coupled equations (36) and (37). Combined with that, the mixed-dimensional model enables an extremely efficient and robust simulation. With both of the fields being solved for separately while the respective other field is frozen, this also enables the independent treatment of the displacement field and the phase-field. This is why for the mixed-dimensional model, the standard procedures for isogeometric discretization and linearization of the weak forms can be employed which in turn is omitted here. A continuous storing and updating of all coupling quantities between the coupled fields is of prominent importance during the solution procedure, which is presented next.

3.2 | Transfer of coupling quantities between geometric spaces

As the descriptions of the phase-field and the displacement field refer to different geometric entities, two separate FE discretizations for the 3D phase-field as well as the 2D shell are needed. For the FE code, this implies that the actual structure has to be discretized once with shell elements and once with solid elements.

For an understanding of the coupling of these with each other, two key facts need to be explained foremost. First, the computation of the stress resultants (35b) is performed by numerical integration along the thickness direction of the shell element. The emanating thickness integration loop is necessary due to non-linear integrands which in turn are due to the thickness-varying tension-compression split of the stress tensor $\sigma^\pm(\Theta^3)$ as well as the phase-field degradation of the stress tensor which is also varying over the thickness with $g[c(\Theta^3)]$. It is worth mentioning that for the case that an isotropic phase-field model is applied, meaning that no tension-compression split is performed, the thickness-integration of the strain energy density and the stress resultants could be done analytically without the need for numerical integration along the thickness direction. This however would still raise the question of how to incorporate the thickness-varying degradation due to the underlying thickness-varying phase-field variable. Nevertheless, the herein adopted shell model together with the phase-field model entailing the tension-compression split is still 2D since the necessary thickness integration loop does include neither a discretization in the thickness direction nor the evaluation of additional shape functions. This means that for this integration loop, multiple quadrature points (QPs) are necessary along the thickness direction of the shell. The second key point for an understanding of the mixed-dimensional coupling is the fact that the exchange of the coupling quantities (to recall, these are c and Ψ_u^+) takes place at the QP level during the element-wise computation of the stiffness matrices and force vectors, as illustrated in Figure 4.

With these two facts established, only now it is reasonable that the QPs of the shell thickness integration loop can be allocated with the regular QPs of the solid element, see Figure 4, to allow the exchange of the coupling quantities between the structural elements and the continuum elements. The exchange of the coupling quantities can also be seen in the pseudo-code Algorithm 1, together with all other relevant sequences of the procedure.

Algorithm 1. Pseudo-code with the sequences relevant for the coupling of the elements

<p>(a) Shell element routine</p> <pre> for <i>shell_element</i> in <i>shell_elements</i> for <i>area_QP</i> in <i>area_QPs</i> for <i>thickness_QP</i> in <i>thickness_QPs</i> get $c(\Theta^3)$ from <i>solid element</i> stress computation spectral decomposition: $\sigma^\pm(\Theta^3)$ degradation: $\sigma(\Theta^3) = g[c(\Theta^3)] \sigma^+(\Theta^3) + \sigma^-(\Theta^3)$ strain energy density computation: $\Psi_u^+(\Theta^3)$ save $\Psi_u^+(\Theta^3)$ for <i>solid element</i> end for end for end for </pre>	<p>(b) Volume element routine</p> <pre> for <i>volume_element</i> in <i>volume_elements</i> for <i>volume_QP</i> in <i>volume_QPs</i> get $\Psi_u^+(\Theta^3)$ from <i>shell element</i> history variable: $\mathcal{H}(\Theta^3) = \max_{\tau < t} [\Psi_u^+(\Theta^3, \tau)]$ interpolate c_i^e from nodes to QP save $c(\Theta^3)$ for <i>shell element</i> end for end for </pre>
---	---

Ultimately, this coupling exhibits itself in one crucial requirement for the two separate discretizations of the structure with shell and solid elements: for each QP of a solid element, there has to be a corresponding QP of the thickness integration loop allocated to the shell element at exactly the same geometrical location. Therewith, it is conceivable to use an

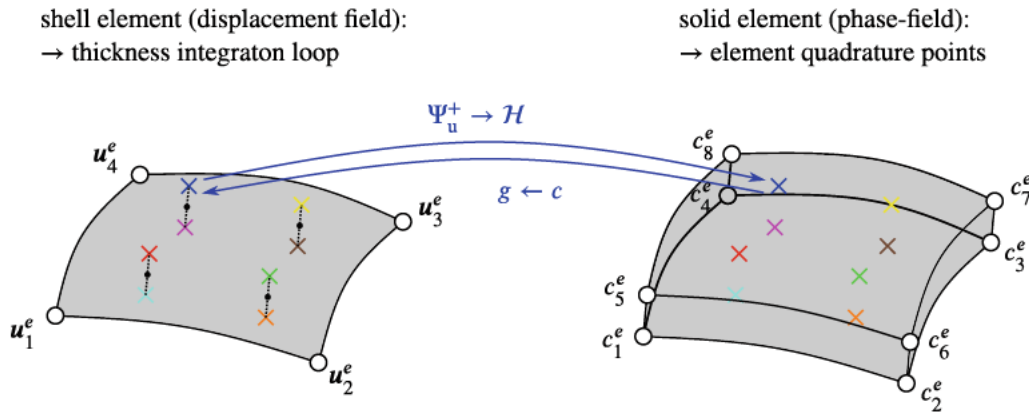


FIGURE 4 Transfer of the coupling quantities between shell and solid element (points: nodes; crosses: quadrature points)

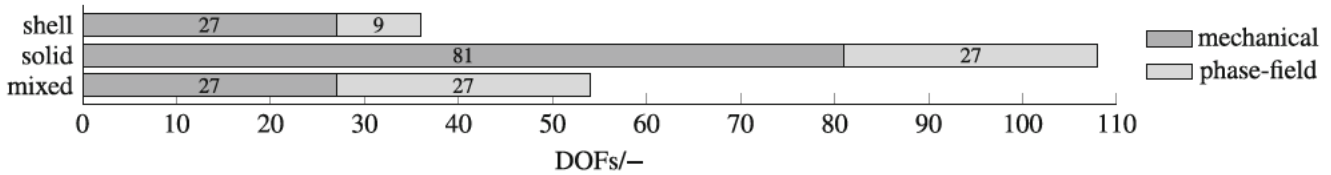


FIGURE 5 Comparison of the total number of degrees of freedom for one element

arbitrarily high element order or even multiple elements in the thickness direction for the phase-field solid element as long as the mentioned condition of spatially coinciding QPs is satisfied. However, in order to narrow down the scope of this article which is intended to be the initial presentation of the proposed model, only one element is used to discretize the thickness direction of the plates and shells in the following numerical examples. Not only that the implementation thereof is most convenient in regards to the coupling of the QPs, additionally this also provides a better comparability to other approaches. Furthermore, NURBS basis functions of third order are used in this article for the elements resulting in 9 area- respectively 27 volume-QPs. As it will also be pointed out later, further research on the proposed model should involve the investigation on multiple element orders in combination with various numbers of elements to discretize the thickness direction.

The comparison of the resulting number of nodal DOFs for one element of the mixed-dimensional model when compared to the shell model and the solid model is depicted in Figure 5 for this explained setup. It can be seen that an element of the mixed-dimensional model has only half of the total DOFs when compared to an element of the solid model and only 50% more total DOFs when compared to an element of the shell model. Comparing the number of QPs for the mentioned setup with third order basis functions, the solid, the mixed-dimensional as well as the shell model all require a total of 27 QPs. As explained previously, this is what allows to transfer the variables between the QPs for the mixed-dimensional model, while the fact that no additional QPs need to be introduced also represents one main strength of the new model.

4 | NUMERICAL EXAMPLES

In the Section 4, various numerical examples are presented to prove the mixed-dimensional models' advantages and to compare it to the solid and shell model. In the comparisons, the results of the solid model act as reference for all the simulations. The key focus of this section is to illustrate the evolution of cracks along the thickness direction of plates and shells. Furthermore, special attention is paid to the influence of the ratio of the length scale parameter to the shell thickness l/t during the investigations on fracture along the thickness direction, because it emphasizes the differences between the compared models. The combinations $l/t \in \{1/1, 1/2, 1/3, 1/4, 1/8, 1/10, 1/20\}$ are chosen for the simulations ranging from a length scale which is hardly able to show a thickness-varying behavior to a very fine length scale.

4.1 | Simply supported beam

With this first example being a simply supported beam whose setup is taken from Reference 32, the aim is to gain detailed insight into the evolution of cracks through the thickness of structural elements. The setup features a rectangular, plane specimen of length $l_1 = 10$ mm and width of $l_2 = 2$ mm without any initial cracks. The $t = 0.025$ mm thin plate is subjected to a constant, normal surface load \bar{p} acting on the complete plate; the geometric properties and boundary conditions of the specimen are shown in Figure 6. In this example, the material parameters are $G_c = 3$ N/mm, $E = 10 \times 10^9$ N/mm² and $\nu = 0.0$ while the latter justifies to refer to the example as beam because the results are constant along the width direction. For the numerical solution, a mesh comprising 18,117 elements initially refined in the region of the expected crack is employed while the simulation is performed with an arc-length control method. At the node located in the middle of the beam, the transverse displacement u_z is traced.

For various length scale parameters, Figure 7 presents the load-displacement curves obtained with the solid, the shell and the mixed-dimensional model. Clearly, the curves depict that with smaller ratios for l/t , the differences between the three compared models become more distinctive. While with $l/t \rightarrow 1$, all of the models produce similar force-displacement curves, with $l/t \rightarrow 1/10$, the mixed-dimensional and solid model show very good agreement while the shell model shows larger deviations from the reference results. The deviations of the shell model are due to the fact that it is not capable to reproduce the thickness-varying behavior of the phase-field which—as stated in the introduction and in Figure 1—starts to evolve from the bottom of the plate. This behavior, together with the influence of the length scale parameter can be seen in Figure 8. Furthermore, while the simulation with $l/t = 1$ virtually shows no variation of the phase-field over the thickness, the smaller length scale parameters show an increasing angle of the damage transitioning zone. Moreover, the results of the simulations featuring a very small ratio l/t clearly show the effect of the adopted strain energy density split in the phase-field model. On the bottom, where tension is predominant, the crack driving force leads to the evolution of the phase-field whereas on the top, where compression occurs, the beam stays intact when the influence of the bottom is not “smeared” towards the top with a small length scale parameter. This case of a beam broken only partly along the thickness direction raises the question of how the system establishes its equilibrium state when considering the linear ansatz for the strain and stress. The numerical results show that the system achieves this by featuring membrane action which in turn results in non-vanishing membrane stress terms despite of the load case comprising bending exclusively. A more detailed explanation of this phenomenon as well as an analytical derivation proving this aspect is presented in Appendix A.

To further illustrate the pivotal thickness-varying behavior of the phase-field and to underscore the initially stated necessity of a more complex phase-field model for shells in the first place, the phase-field variable c (Θ^i) is plotted against the width as well as the thickness direction of the plate in Figure 9. The phase-field variable as obtained with the shell and solid model is plotted therein as well for comparison purposes. Again, the simulations with $l/t \rightarrow 1$ show almost no variation along the z -direction whereas the simulations with $l/t \rightarrow 1/10$ clearly show one. The mixed-dimensional model produces results which are almost identical to those of the solid model which emphasizes the big advantage of

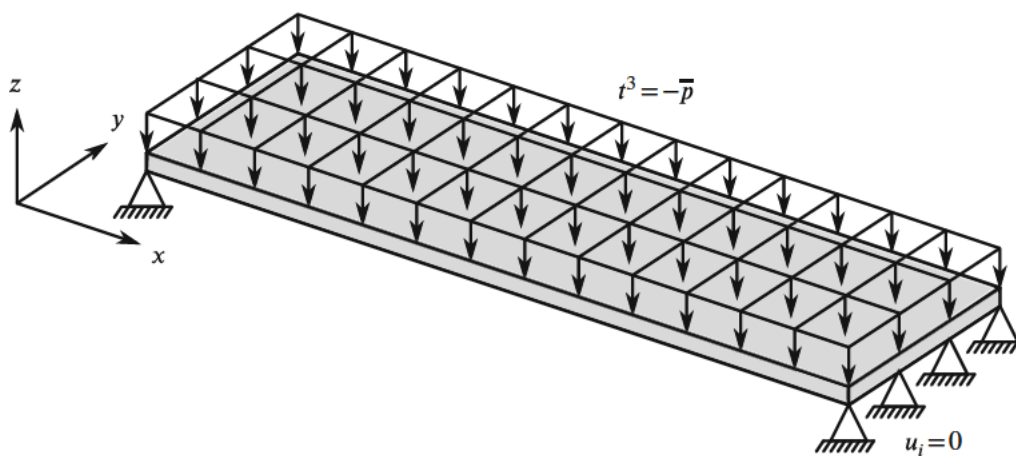


FIGURE 6 Simply supported beam, setup

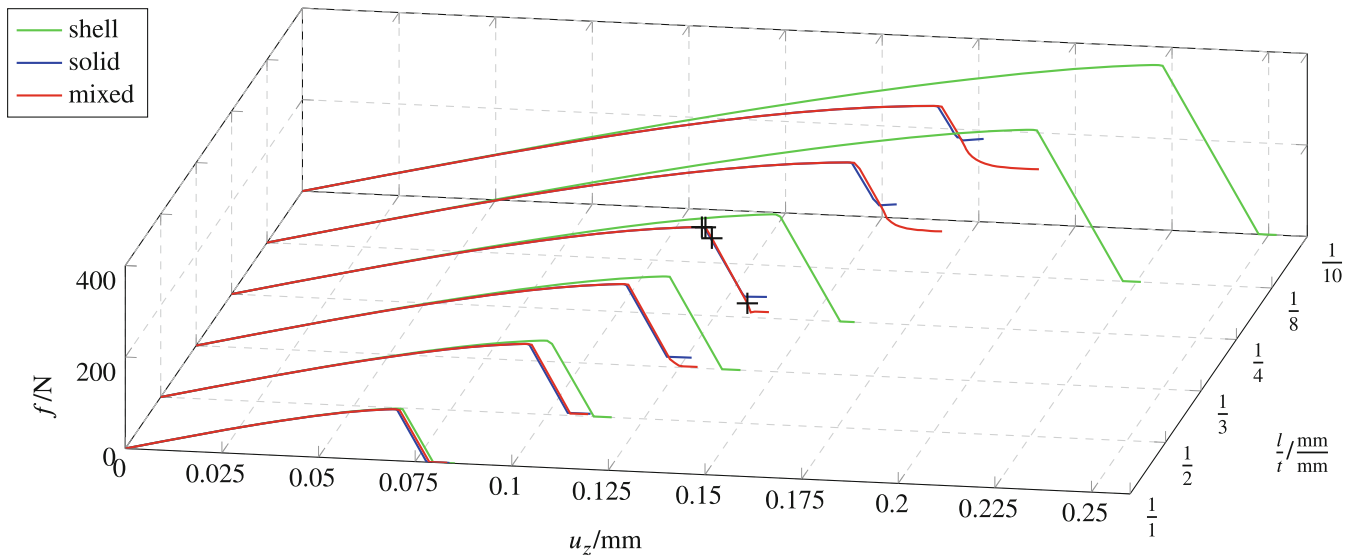


FIGURE 7 Simply supported beam, force-displacement curves



FIGURE 8 Simply supported beam, final phase-field as obtained with the mixed-dimensional model (side view). (A) $l/t = 1/1$; (B) $l/t = 1/2$; (C) $l/t = 1/3$; (D) $l/t = 1/4$; (E) $l/t = 1/8$; (F) $l/t = 1/10$

the proposed model since it is still able to accurately depict the through-thickness crack evolution whilst entailing significantly reduced computational cost in terms of required DOFs compared to solid elements. All in all, these plots clearly underscore the ability of the mixed-dimensional model to reproduce the thickness-varying phase-field of the reference.

The observed agreement of mixed-dimensional and solid model is further reinforced when comparing the evolution of the phase-field variable over the transverse displacement u_z , as Figure 10A shows representatively for $l/t = 1/4$. The plot once again emphasizes that the mixed-dimensional model is able to precisely reproduce the phase-field evolution of the solid model at various points along the thickness direction (top, middle, and bottom of the beam). Furthermore, Figure 10B–E illustrates the phase-field variable as obtained with the mixed-dimensional model for $l/t = 1/4$ at various evolution stages around the peak loading point to proof a further advantage of the new model over the shell model.

The new model now also comes with the possibility to model shells that feature an initial crack which is ranging only partly through the thickness of the shell. For this purpose, the same setup as before—only with the slight modification that the bottom side features the initial crack, which is induced as shown in Reference 70—is considered for the mixed-dimensional and the solid model. As the shell model cannot depict such a crack, it will not serve as object

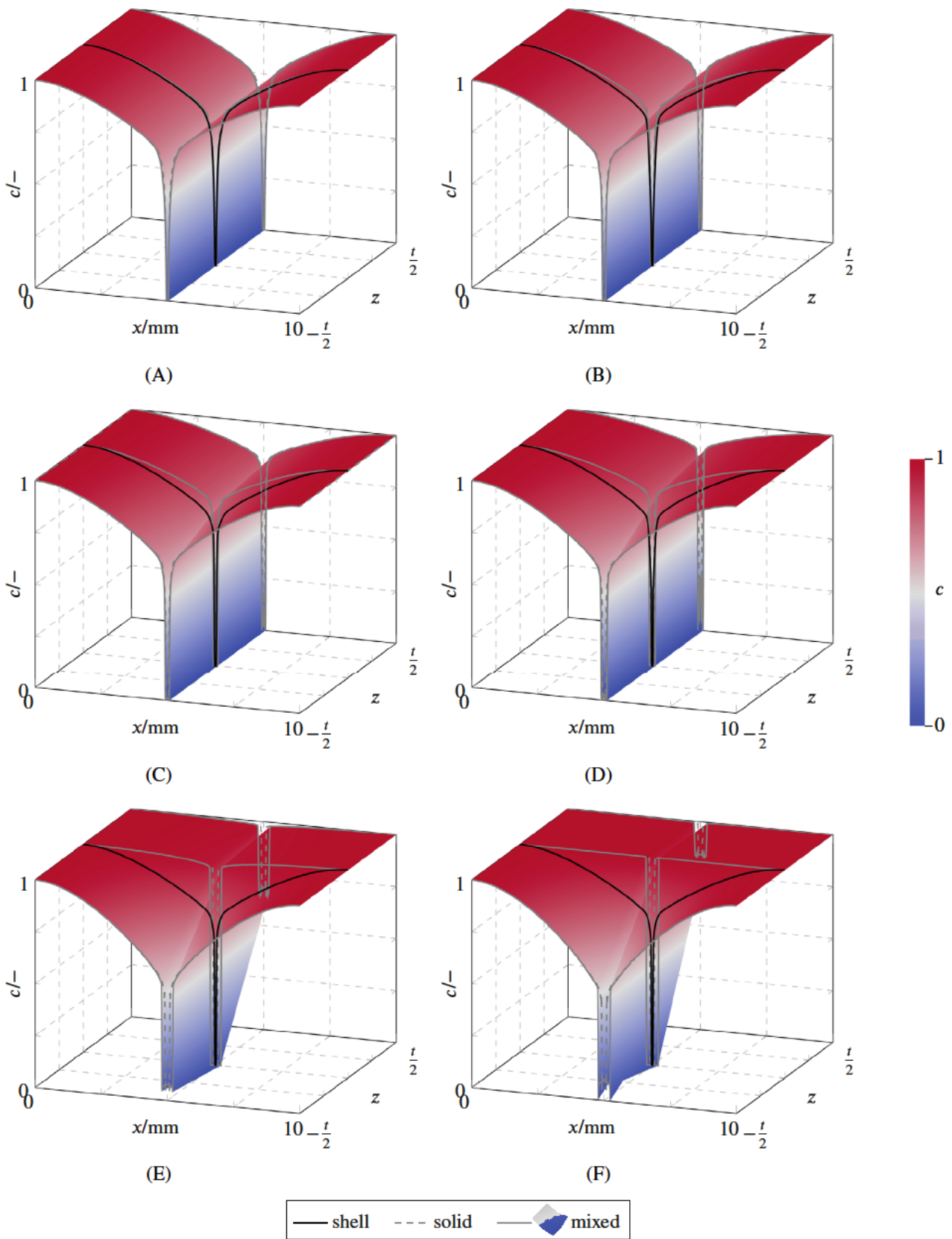


FIGURE 9 Simply supported beam, final phase-field variable c plotted against the length direction x and the thickness direction z at width $y = 0$ mm. (A) $l/t = 1/1$; (B) $l/t = 1/2$; (C) $l/t = 1/3$; (D) $l/t = 1/4$; (E) $l/t = 1/8$; (F) $l/t = 1/10$

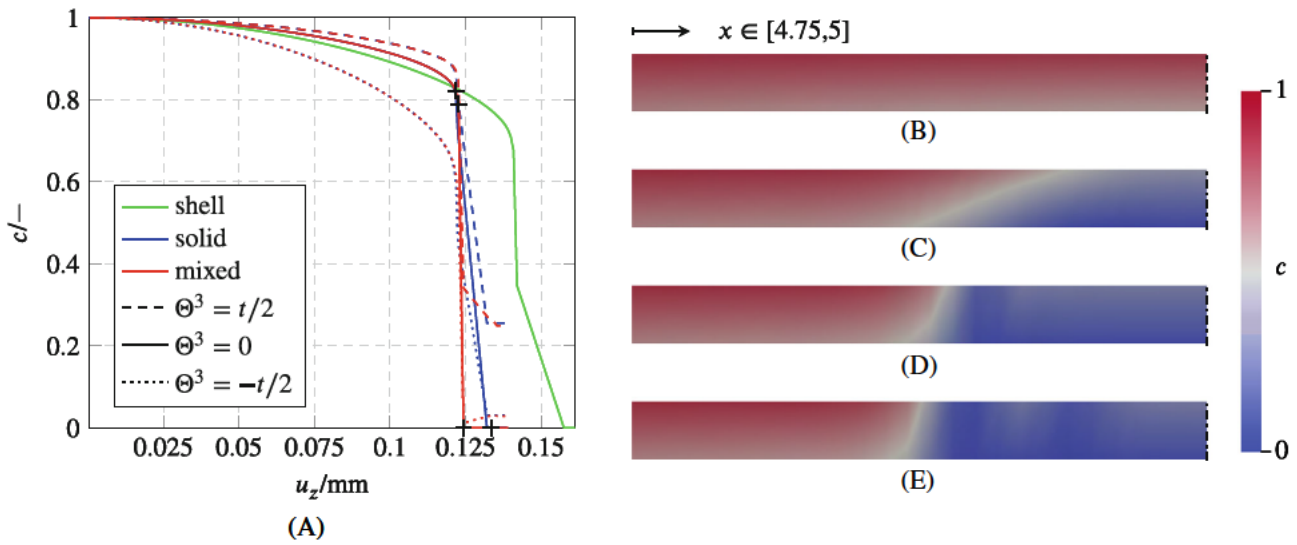


FIGURE 10 Simply supported beam, phase-field evolution over the thickness for $l/t = 1/4$. (A) Phase-field variable over the max. displacement; (B) Phase-field at $u_z = 0.121\ 69\ \text{mm}$, $f = 192.87\ \text{N}$; (C) phase-field at $u_z = 0.122\ 61\ \text{mm}$, $f = 192.73\ \text{N}$; (D) phase-field at $u_z = 0.124\ 27\ \text{mm}$, $f = 169.45\ \text{N}$; (E) phase-field at $u_z = 0.133\ 46\ \text{mm}$, $f = 30.723\ \text{N}$; The stages (B)–(E) refer to the + marks in (A) and Figure 7

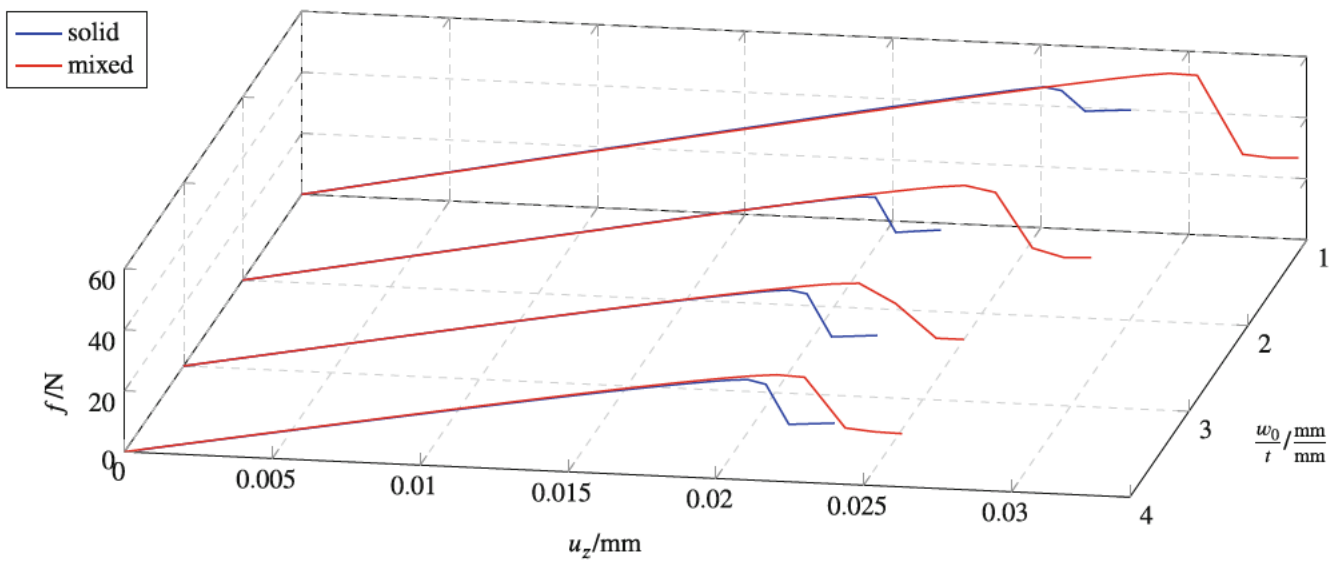


FIGURE 11 Initially partly broken beam, force-displacement curves

of comparison here. For this simulation with an initial crack, a length scale parameter to thickness ratio $l/t = 1/4$ is used.

The force-displacement curves, showing the influence of the initial crack width w_0 (as evoked by an initial history variable distribution, see the approach presented in Reference 29) for the ratios $w_0/t = \{1, 2, 3, 4\}$ are given in Figure 11. It can clearly be observed that the beams with a wider initial crack need less external loading to fully crack along the thickness direction than the ones with a tighter initial crack. Evidently, the mixed-dimensional model is again able to resemble the results obtained with the solid model, with a smaller initial crack width the differences between the models become more evident however. The initial as well as the final phase-field distributions are shown for the various ratios w_0/t in Figure 12. Therein, it can be seen that the crack keeps its width as well as the angle of the phase-field transition zone as the crack evolves along the thickness direction.

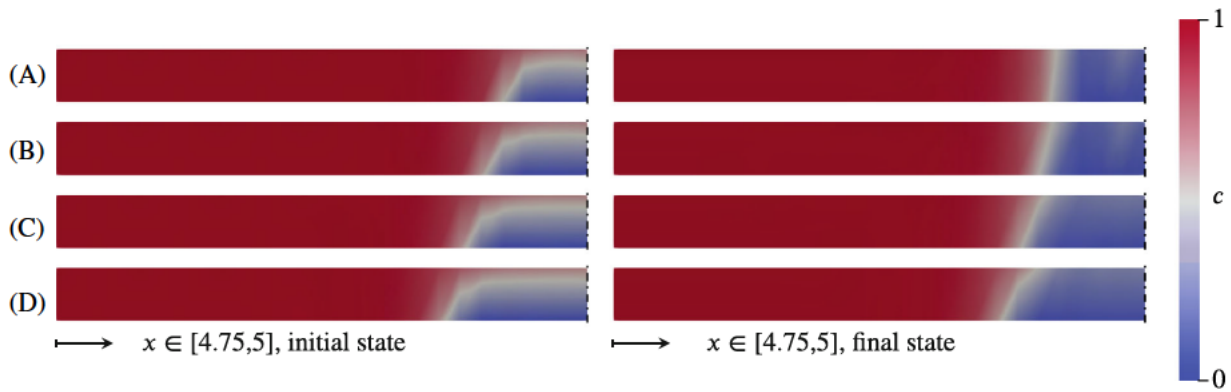


FIGURE 12 Initially partly broken beam, initial and final phase-field as obtained with the mixed-dimensional model (side view). (A) $w_0/t=1$; (B) $w_0/t=2$; (C) $w_0/t=3$; (D) $w_0/t=4$

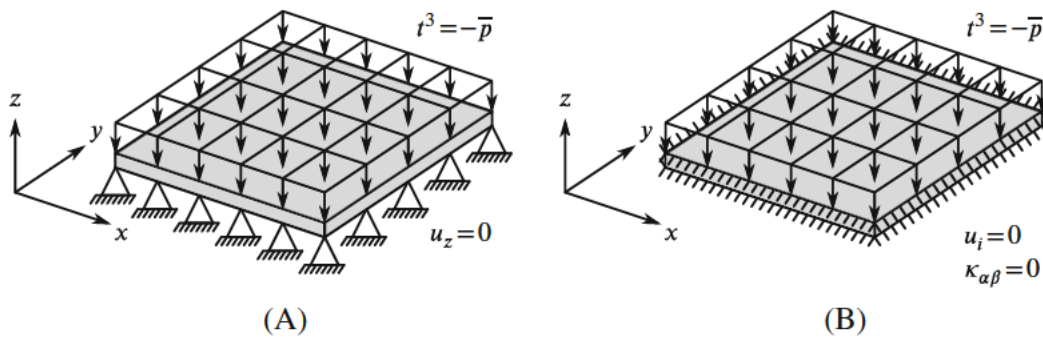


FIGURE 13 Plate setup. (A) Simply supported edges; (B) clamped edges

4.2 | Simply supported and clamped plate

In the next example, an quadratic plate under a constant transverse surface load \bar{p} is considered. The aim with this example is to investigate the impact of the through-thickness crack evolution on the crack path. To do so, two test cases with simply supported and clamped edges around the plate are employed to examine the crack paths predicted by the models.

The plate has the dimensions $l_1 = l_2 = 1$ mm and a thickness of $t = 0.02$ mm, the resulting setups including the boundary conditions are illustrated in Figure 13. As material parameters, $E = 190 \times 10^3$ N/mm², $\nu = 0.29$ and $\mathcal{G}_c = 0.295$ N/mm are used. Since the resulting fields are symmetric to the x - as well as the y -axis, only a quarter of the plate with respective symmetry boundary conditions is simulated with an uniform mesh comprising 22,801 elements. For coherent comparison purposes, the EUCLIDIAN norm of the displacement field divided by the number of control points $\|\mathbf{u}\|/n_{CP}$ is monitored in each step. The normalization with n_{CP} serves the comparability between the models of various dimensionality.

The resulting force-displacement curves obtained with both setups, for the different models as well as the various ratios l/t are given in Figure 14. Figure 15 shows the resulting, final phase-field as obtained with the mixed-dimensional model with $l/t = 1/4$ not only from a top view, but also in side views respectively in a diagonal cut. The latter really show the phase-field evolution along the thickness direction and thereby again emphasizes the necessity to consider the phase-field variable as not constant through the thickness. The results confirm the same observations of the first numerical example. A comparison of the crack paths underscores that the proposed mixed-dimensional model is not only able to accurately reproduce the crack path with respect to the shell midsurface, but in contrast to the shell model is additionally able to accurately reproduce the phase-field evolution in the thickness direction of the reference model, for example, where the crack initiates with respect to the thickness coordinate.

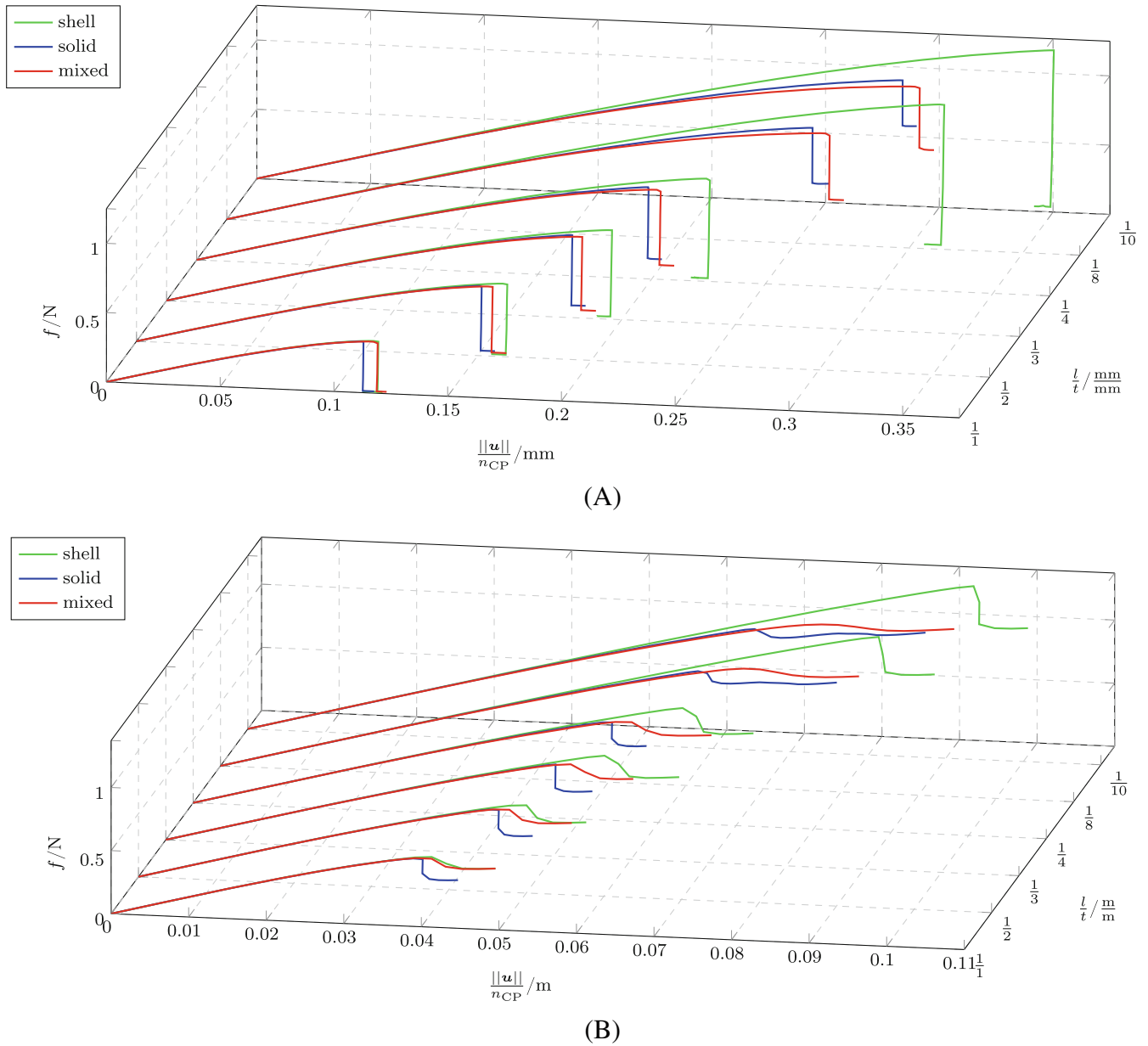


FIGURE 14 Simply supported and clamped plate, force-displacement curves. (A) Simply supported edges; (B) clamped edges

4.3 | Notched hemisphere

For the final example, the aim is to extend the precedent investigations and insights to a shell with a curved geometry. This curved geometry additionally features an initial crack which is ranging only partly over the thickness. For this purpose, a hemisphere of radius $r = 10$ mm and thickness $t = 0.5$ mm under uniform internal pressure as illustrated in Figure 16 is considered whereas the material parameters are $E = 2.1 \times 10^5$ N/mm², $\nu = 0.25$ and $G_c = 2.7$ N/mm. Again, taking advantage of the symmetry of the problem, only an eighth of the hemisphere with respective boundary conditions is simulated. Two initial cracks only partly through the thickness running of length $a_0 = 1$ mm are situated under an angle of 90° ultimately forming a cross pattern at the upper inside of the hemisphere. These initial cracks range from one side to only the first third of the shell thickness, analogously to the initially partly broken beam. Since the shell model is not able to represent any initial cracks ranging only partly through the thickness, it will not be considered in this numerical example.

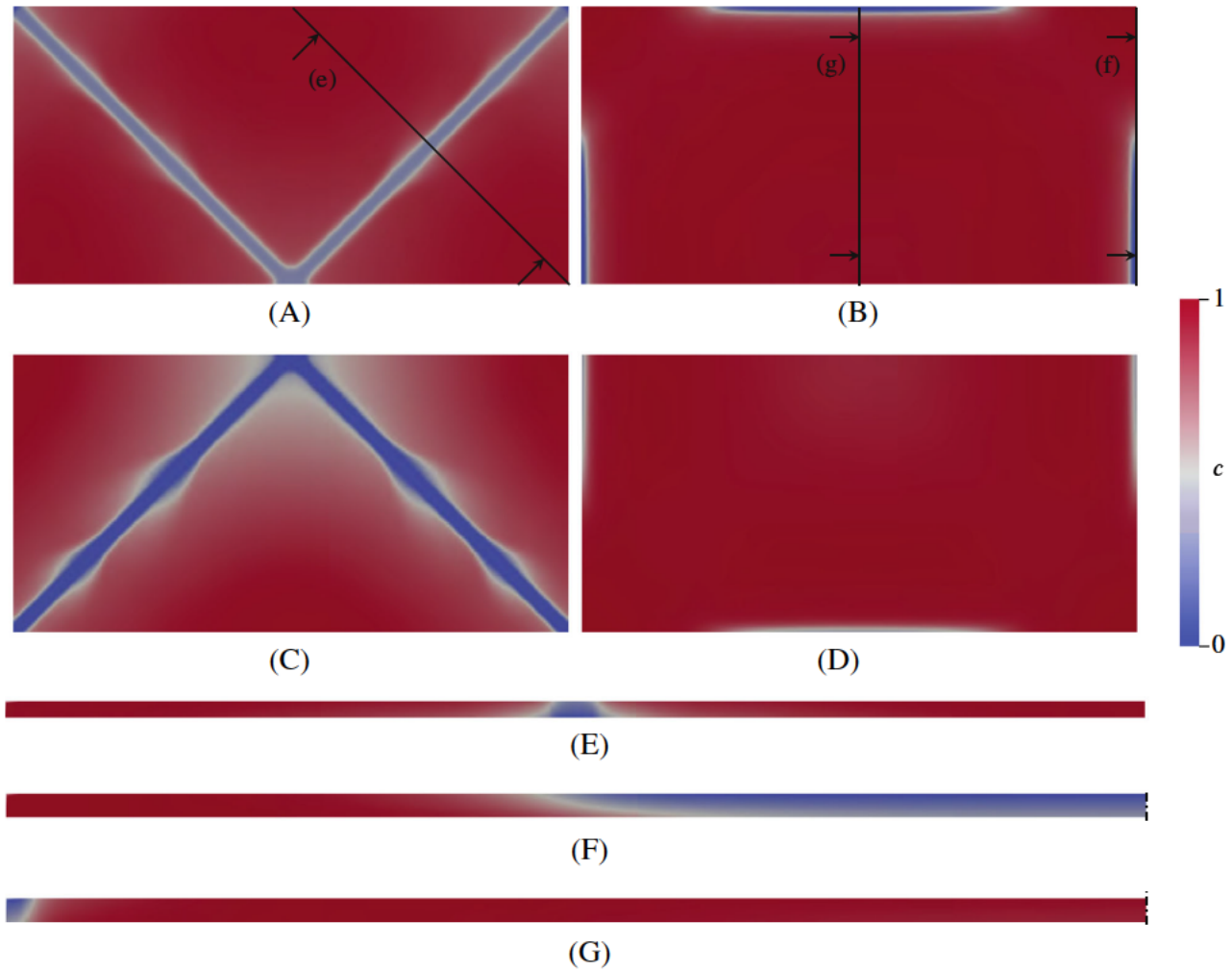


FIGURE 15 Simply supported and clamped plate, final phase-field as obtained with the mixed-dimensional model for $l/t = 1/4$. (A) Simply supported edges (half, top view); (B) clamped edges (half, top view); (C) simply supported edges (half, bottom view); (D) clamped edges (half, bottom view); (E) simply supported edges (diagonal cut perpendicular to one of the crack paths); (F) clamped edges (side view normal to one of the crack paths); (G) clamped edges (side view perpendicular to one of the cracks paths)

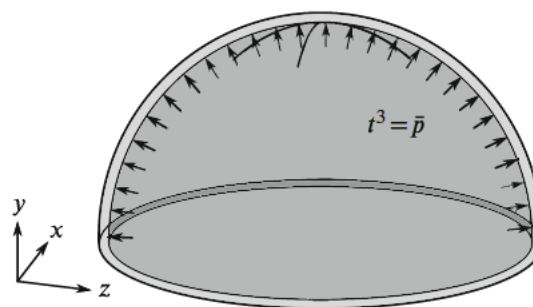


FIGURE 16 Notched hemisphere, setup

Both of the models show a very similar behavior of the force-displacement curve for the investigated ratios $l/t = \{1/4, 1/8, 1/10, 1/20\}$, see Figure 17: the first critical point is hit when the initial, only partly through the thickness ranging cracks advanced along the thickness direction such that they reach the opposite side of the shell. The evolution along the thickness direction takes place before the cracks evolve along the shell midsurface. From this point on, the cracks grow towards the equator of the hemisphere keeping the initial cross-pattern while the phase-field crack on the outside henceforth stays marginally ahead of the phase-field crack on the inside. The simulation is stopped at the shown

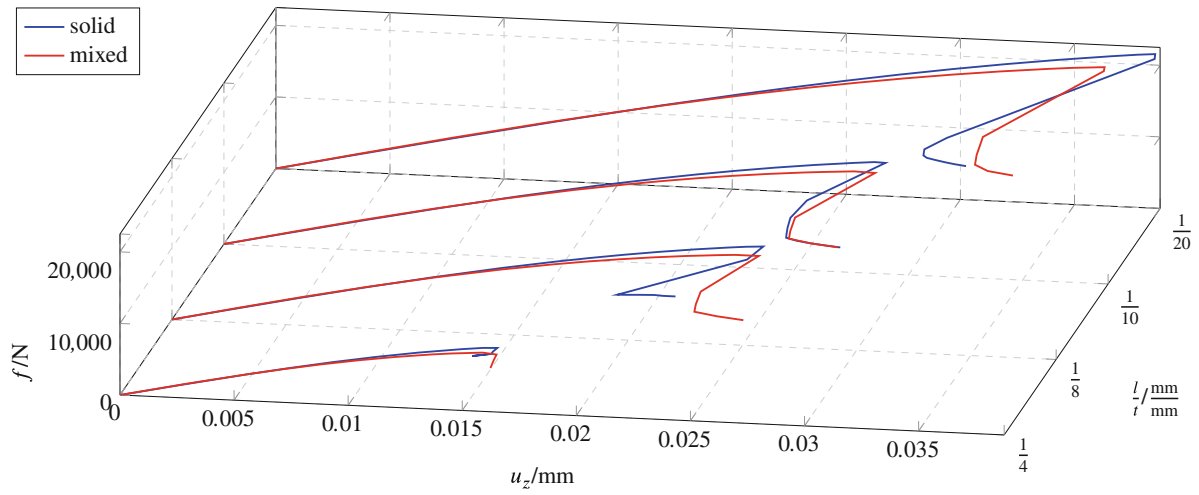


FIGURE 17 Notched hemisphere, force-displacement curves

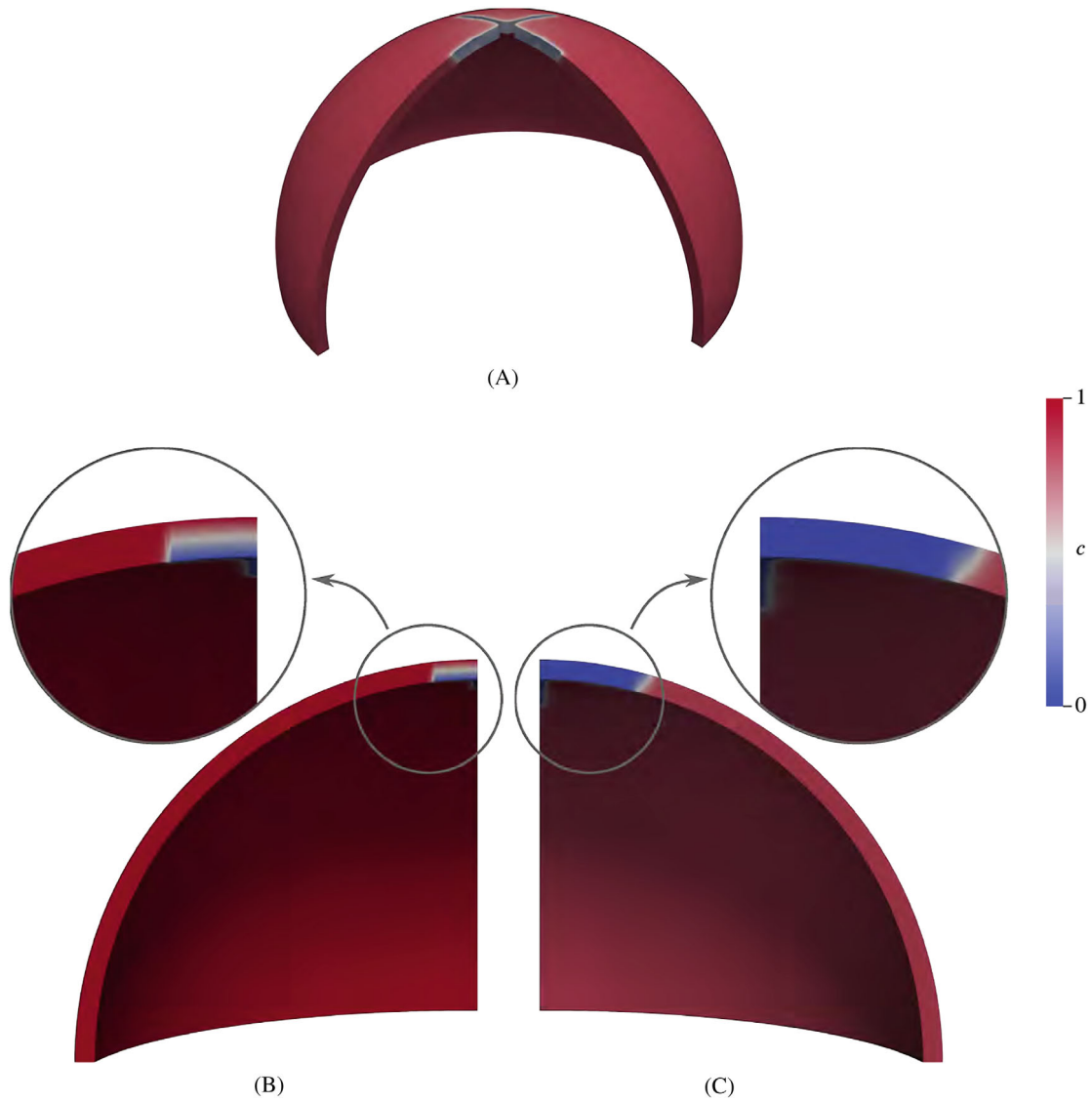


FIGURE 18 Notched hemisphere, phase-field as obtained with the mixed-dimensional model for $l/t = 1/10$. (A) Three-quarter, final state with elements $c \leq 0.25$ hidden; (B) quarter, initial state; (C) quarter, final state

points in Figure 17 due to the first distinctive points in the force-displacement curves already met as well as the limit of the small deformation prerequisite being hit. The phase-field can be seen in Figure 18 in various stages and views.

5 | CONCLUSIONS

In this article, a new model is introduced to deal with phase-field brittle fracture along the thickness direction of thin plates and shells in a computationally efficient manner.

This new mixed-dimensional model combines a 2D representation of the displacement field (in this article exemplary formulated with KL shell kinematics), with a 3D phase-field description. For the implementation, which is based on IGA due to the thereby possible rotation-free shell formulation in this article, the mixed-dimensional model necessitates in two separate FE discretizations. One of them features shell elements with the displacement DOFs as well as a thickness integration loop while the other one entails volume elements with the phase-field DOFs. Both of them are coupled by an exchange of the coupling quantities at the QP which hence need to have corresponding geometric locations. With this proposed mixed-dimensional model, arbitrary phase-field behavior along the thickness direction can be approximated without any assumptions or simplifications for the phase-field being necessary. This clearly lets the proposed model stand out from previous approaches to phase-field fracture of plates and shells which usually consider the phase-field variable to be constant along the thickness direction. All this is while the newly introduced model has significantly reduced computational cost when compared to the 3D model while also featuring additional capabilities such as the capability to model initial cracks which are ranging only partly over the shell thickness or phase-field gradients in the thickness direction. The results of various numerical examples show that the mixed-dimensional model in fact is capable of accurately reproducing the results of a standard (fully 3D) solid model while also indicating that the consideration of the phase-field as varying over the thickness is in fact necessary. Furthermore, the simulations in this article illustrate the tremendous impact of the ratio of the length scale parameter to the shell thickness on the phase-field behavior in the thickness direction.

With this first paper only acting as initial presentation of the mixed-dimensional model, there are many feasible extensions to it which are yet to be investigated, such as: the extension to large strains and plasticity or other shell kinematics, the application of the model to other coupled field problems and the combination with local refinement techniques such as applied in Reference 71. An investigation on the phase-field behavior with more than three thickness integration points or more than one thickness element also promises valuable insights in future work.

ACKNOWLEDGMENTS


This work was supported by the Deutsche Forschungsgemeinschaft (DFG) via the project “Experimental analysis and phase-field modeling of the interaction between plastic zone and fatigue crack growth in ductile materials under complex loading” (Grant number KA 3309/12-1).

Furthermore, the authors are grateful to the Centre for Information Services and High Performance Computing [Zentrum für Informationsdienste und Hochleistungsrechnen (ZIH)] TU Dresden for providing its facilities for high throughput calculations. Finally, the authors gratefully want to acknowledge the helpful discussions with Jörg Brummund.

DATA AVAILABILITY STATEMENT

The data that support the findings of this study are available from the corresponding author upon reasonable request.

ORCID

Markus Kästner  <https://orcid.org/0000-0003-3358-1545>

REFERENCES

1. Yuan Y, Tan P. Deformation and failure of rectangular plates subjected to impulsive loadings. *Int J Impact Eng*. 2013;59:46-59. doi:10.1016/j.ijimpeng.2013.03.009
2. Moes N, Dolbow J, Belytschko T. A finite element method for crack growth without remeshing. *Int J Numer Meth Engng*. 1999;46:131-150.
3. Areias PMA, Belytschko T. Non-linear analysis of shells with arbitrary evolving cracks using XFEM. *Int J Numer Methods Eng*. 2005;62(3):384-415. doi:10.1002/nme.1192

4. Dolbow J, Mo N. Modeling fracture in Mindlin-Reissner plates with the extended finite element method. *Int J Solids Struct.* 2000;37:7161-7183.
5. Larsson R, Mediavilla J, Fagerström M. Dynamic fracture modeling in shell structures based on XFEM: dynamic fracture modeling based on XFEM. *Int J Numer Methods Eng.* 2011;86(4-5):499-527. doi:10.1002/nme.3086
6. Nguyen-Thanh N, Valizadeh N, Nguyen M, et al. An extended isogeometric thin shell analysis based on Kirchhoff-Love theory. *Comput Methods Appl Mech Eng.* 2015;284:265-291. doi:10.1016/j.cma.2014.08.025
7. Amiri F, Millán D, Shen Y, Rabczuk T, Arroyo M. Phase-field modeling of fracture in linear thin shells. *Theor Appl Fract Mech.* 2014;69:102-109. doi:10.1016/j.tafmec.2013.12.002
8. Li W, Nguyen-Thanh N, Huang J, Zhou K. Adaptive analysis of crack propagation in thin-shell structures via an isogeometric-meshfree moving least-squares approach. *Comput Methods Appl Mech Eng.* 2020;358:112613. doi:10.1016/j.cma.2019.112613
9. Peng YX, Zhang AM, Ming FR. A 3D meshfree crack propagation algorithm for the dynamic fracture in arbitrary curved shell. *Comput Methods Appl Mech Eng.* 2020;367:113139. doi:10.1016/j.cma.2020.113139
10. Griffith AA. The phenomena of rupture and flow in solids. *Philos Trans Royal Soc Lond.* 1921;221(582-593):37.
11. Francfort G, Marigo JJ. Revisiting brittle fracture as an energy minimization problem. *J Mech Phys Solids.* 1998;46(8):1319-1342. doi:10.1016/S0022-5096(98)00034-9
12. Bourdin B, Francfort G, Marigo JJ. Numerical experiments in revisited brittle fracture. *J Mech Phys Solids.* 2000;48(4):797-826. doi:10.1016/S0022-5096(99)00028-9
13. Ambati M, Gerasimov T, De Lorenzis L. A review on phase-field models of brittle fracture and a new fast hybrid formulation. *Comput Mech.* 2015;55(2):383-405. doi:10.1007/s00466-014-1109-y
14. Ambati M, Gerasimov T, De Lorenzis L. Phase-field modeling of ductile fracture. *Comput Mech.* 2015;55(5):1017-1040. doi:10.1007/s00466-015-1151-4
15. Miehe C, Aldakheel F, Raina A. Phase field modeling of ductile fracture at finite strains: a variational gradient-extended plasticity-damage theory. *Int J Plast.* 2016;84:1-32. doi:10.1016/j.ijplas.2016.04.011
16. Shen R, Waisman H, Guo L. Fracture of viscoelastic solids modeled with a modified phase field method. *Comput Methods Appl Mech Eng.* 2019;346:862-890. doi:10.1016/j.cma.2018.09.018
17. Dammaß F, Ambati M, Kästner M. A unified phase-field model of fracture in viscoelastic materials. *Contin Mech Thermodyn.* 2021;33(4):1907-1929. doi:10.1007/s00161-021-01013-3
18. Hansen-Dörr AC, de Borst R, Hennig P, Kästner M. Phase-field modelling of interface failure in brittle materials. *Comput Methods Appl Mech Eng.* 2019;346:25-42. doi:10.1016/j.cma.2018.11.020
19. Dammaß F, Hansen-Dörr AC, Kästner M. Phase-field simulation of crack propagation at adhesive interfaces in brittle materials. *PAMM.* 2021;20(1):e202000211. doi:10.1002/pamm.202000211
20. Carollo V, Guillén-Hernández T, Reinoso J, Paggi M. Recent advancements on the phase field approach to brittle fracture for heterogeneous materials and structures. *Adv Model Simul Eng Sci.* 2018;5(1):8. doi:10.1186/s40323-018-0102-y
21. Hansen-Dörr AC, Dammaß F, de Borst R, Kästner M. Phase-field modeling of crack branching and deflection in heterogeneous media. *Eng Fract Mech.* 2020;232:107004. doi:10.1016/j.engfracmech.2020.107004
22. Borden MJ, Verhoosel CV, Scott MA, Hughes TJ, Landis CM. A phase-field description of dynamic brittle fracture. *Comput Methods Appl Mech Eng.* 2012;217-220:77-95. doi:10.1016/j.cma.2012.01.008
23. Ren H, Zhuang X, Anitescu C, Rabczuk T. An explicit phase field method for brittle dynamic fracture. *Comput Struct.* 2019;217:45-56. doi:10.1016/j.compstruc.2019.03.005
24. Seiler M, Linse T, Hantschke P, Kästner M. An efficient phase-field model for fatigue fracture in ductile materials. *Eng Fract Mech.* 2020;224:106807. doi:10.1016/j.engfracmech.2019.106807
25. Seleš K, Aldakheel F, Tonković Z, Sorić J, Wriggers P. A general phase-field model for fatigue failure in brittle and ductile solids. *Comput Mech.* 2021;67(5):1431-1452. doi:10.1007/s00466-021-01996-5
26. Carrara P, Ambati M, Alessi R, De Lorenzis L. A novel framework to model the fatigue behavior of brittle materials based on a variational phase-field approach. *Comput Methods Appl Mech Eng.* 2020;361:112731. doi:10.1016/j.cma.2019.112731
27. Gültekin O, Dal H, Holzapfel GA. Numerical aspects of anisotropic failure in soft biological tissues favor energy-based criteria: a rate-dependent anisotropic crack phase-field model. *Comput Methods Appl Mech Eng.* 2018;331:23-52. doi:10.1016/j.cma.2017.11.008
28. Nagaraja S, Leichsenring K, Ambati M, De Lorenzis L, Böhl M. On a phase-field approach to model fracture of small intestine walls. *Acta Biomater.* 2021;130:317-331. doi:10.1016/j.actbio.2021.06.002
29. Ulmer H, Hofacker M, Miehe C. Phase field modeling of fracture in plates and shells. *PAMM.* 2012;12(1):171-172. doi:10.1002/pamm.201210076
30. Henry H, Levine H. Dynamic instabilities of fracture under biaxial strain using a phase field model. *Phys Rev Lett.* 2004;93:105504. doi:10.1103/PhysRevLett.93.105504
31. Miehe C, Hofacker M, Welschinger F. A phase field model for rate-independent crack propagation: Robust algorithmic implementation based on operator splits. *Comput Methods Appl Mech Eng.* 2010;199(45-48):2765-2778. doi:10.1016/j.cma.2010.04.011
32. Kiendl J, Ambati M, De Lorenzis L, Gomez H, Reali A. Phase-field description of brittle fracture in plates and shells. *Comput Methods Appl Mech Eng.* 2016;312:374-394. doi:10.1016/j.cma.2016.09.011
33. Kikis G, Ambati M, De Lorenzis L, Klinkel S. A phase-field model of brittle fracture for an isogeometric Reissner-Mindlin shell formulation. *PAMM.* 2019;19(1):e201900311. doi:10.1002/pamm.201900311

34. Kikis G, Ambati M, De Lorenzis L, Klinkel S. Phase-field model of brittle fracture in Reissner–Mindlin plates and shells. *Comput Methods Appl Mech Eng*. 2021;373:113490. doi:10.1016/j.cma.2020.113490
35. Pillai U, Triantafyllou SP, Ashcroft I, Essa Y, de la Escalera FM. IFM. Phase-field modelling of brittle fracture in thin shell elements based on the MITC4+ approach. *Comput Mech*. 2020;65(6):1413–1432. doi:10.1007/s00466-020-01827-z
36. Ambati M, De Lorenzis L. Phase-field modeling of brittle and ductile fracture in shells with isogeometric NURBS-based solid-shell elements. *Comput Methods Appl Mech Eng*. 2016;312:351–373. doi:10.1016/j.cma.2016.02.017
37. Reinoso J, Paggi M, Linder C. Phase field modeling of brittle fracture for enhanced assumed strain shells at large deformations: formulation and finite element implementation. *Comput Mech*. 2017;59(6):981–1001. doi:10.1007/s00466-017-1386-3
38. Proserpio D, Ambati M, De Lorenzis L, Kiendl J. Phase-field simulation of ductile fracture in shell structures. *Comput Methods Appl Mech Eng*. 2021;385:114019. doi:10.1016/j.cma.2021.114019
39. Li B, Millán D, Torres-Sánchez A, Roman B, Arroyo M. A variational model of fracture for tearing brittle thin sheets. *J Mech Phys Solids*. 2018;119:334–348. doi:10.1016/j.jmps.2018.06.022
40. Guillén-Hernández T, Reinoso J, Paggi M. Phase field model for fracture analysis of functionally graded power-based shell structures. *Mech Adv Mater Struct*. 2022;29:78–88. doi:10.1080/15376494.2020.1751354
41. Raghu P, Rajagopal A, Reddy JN. Thermodynamically consistent variational approach for modeling brittle fracture in thick plates by a hybrid phase field model. *J Appl Mech*. 2020;87(2):021002. doi:10.1115/1.4045236
42. Paul K, Zimmermann C, Mandadapu KK, Hughes TJR, Landis CM, Sauer RA. An adaptive space-time phase field formulation for dynamic fracture of brittle shells based on LR NURBS. *Comput Mech*. 2020;65(4):1039–1062. doi:10.1007/s00466-019-01807-y
43. Raghu P, Rajagopal A, Jalan SK, Reddy JN. Modeling of brittle fracture in thick plates subjected to transient dynamic loads using a hybrid phase field model. *Meccanica*. 2021;56(6):1269–1286. doi:10.1007/s11012-020-01224-z
44. Proserpio D, Kiendl J, Ambati M, Lorenzis LD, Andre K, Kvamsdal T. Simulation of brittle fracture in shells using a phase-field approach and LR B-splines. Proceedings of the 7th GACM Colloquium on Computational Mechanics for Young Scientists from Academia and Industry; 2017; German Association for Computational Mechanics, Stuttgart, Germany.
45. Proserpio D, Ambati M, De Lorenzis L, Kiendl J. A framework for efficient isogeometric computations of phase-field brittle fracture in multipatch shell structures. *Comput Methods Appl Mech Eng*. 2020;372:113363. doi:10.1016/j.cma.2020.113363
46. Areias P, Rabczuk T, Msek M. Phase-field analysis of finite-strain plates and shells including element subdivision. *Comput Methods Appl Mech Eng*. 2016;312:322–350. doi:10.1016/j.cma.2016.01.020
47. Lai W, Gao J, Li Y, Arroyo M, Shen Y. Phase field modeling of brittle fracture in an Euler-Bernoulli beam accounting for transverse part-through cracks. *Comput Methods Appl Mech Eng*. 2020;361:112787. doi:10.1016/j.cma.2019.112787
48. Areias PMA, Rabczuk T. Quasi-static crack propagation in plane and plate structures using set-valued traction-separation laws: traction-separation laws. *Int J Numer Methods Eng*. 2008;74(3):475–505. doi:10.1002/nme.2182
49. Kiendl J, Bletzinger KU, Linhard J, Wüchner R. Isogeometric shell analysis with Kirchhoff-Love elements. *Comput Methods Appl Mech Eng*. 2009;198(49–52):3902–3914. doi:10.1016/j.cma.2009.08.013
50. Benson D, Bazilevs Y, Hsu MC, Hughes T. A large deformation, rotation-free, isogeometric shell. *Comput Methods Appl Mech Eng*. 2011;200(13–16):1367–1378. doi:10.1016/j.cma.2010.12.003
51. Radenković G, Borković A, Marussig B. Nonlinear static isogeometric analysis of arbitrarily curved Kirchhoff-Love shells. *Int J Mech Sci*. 2021;192:106143. doi:10.1016/j.ijmecsci.2020.106143
52. Ambati M, Kiendl J, De Lorenzis L. Isogeometric Kirchhoff-Love shell formulation for elasto-plasticity. *Comput Methods Appl Mech Eng*. 2018;340:320–339. doi:10.1016/j.cma.2018.05.023
53. Kiendl J, Hsu MC, Wu MC, Reali A. Isogeometric Kirchhoff-Love shell formulations for general hyperelastic materials. *Comput Methods Appl Mech Eng*. 2015;291:280–303. doi:10.1016/j.cma.2015.03.010
54. Coox L, Maurin F, Greco F, Deckers E, Vandepitte D, Desmet W. A flexible approach for coupling NURBS patches in rotationless isogeometric analysis of Kirchhoff-Love shells. *Comput Methods Appl Mech Eng*. 2017;325:505–531. doi:10.1016/j.cma.2017.07.022
55. Coradello L, Loli G, Buffa A. A projected super-penalty method for the C^1 -coupling of multi-patch isogeometric Kirchhoff plates. *Comput Mech*. 2021;67(4):1133–1153. doi:10.1007/s00466-021-01983-w
56. Kiendl J, Bazilevs Y, Hsu MC, Wüchner R, Bletzinger KU. The bending strip method for isogeometric analysis of Kirchhoff-Love shell structures comprised of multiple patches. *Comput Methods Appl Mech Eng*. 2010;199(37–40):2403–2416. doi:10.1016/j.cma.2010.03.029
57. Schuß S, Dittmann M, Wohlmuth B, Klinkel S, Hesch C. Multi-patch isogeometric analysis for Kirchhoff-Love shell elements. *Comput Methods Appl Mech Eng*. 2019;349:91–116. doi:10.1016/j.cma.2019.02.015
58. Echter R. Isogeometric analysis of shells. PhD Thesis. Stuttgart: Institut für Baustatik und Baudynamik der University of Stuttgart; 2013. .
59. Izzuddin BA, Jokhio GA. Mixed-dimensional coupling for parallel partitioned nonlinear finite-element analysis. *J Comput Civ Eng*. 2017;31(3):04016062. doi:10.1061/(ASCE)CP.1943-5487.0000633
60. Nguyen VP, Kerfriden P, Claus S, Bordas SPA. Nitsche's method method for mixed dimensional analysis: conforming and non-conforming continuum-beam and continuum-plate coupling. arxiv.org/abs/1308.2910. 2013.
61. Rabinovich D, Ofir Y, Givoli D. The Nitsche method applied to a class of mixed-dimensional coupling problems. *Comput Methods Appl Mech Eng*. 2014;274:125–147. doi:10.1016/j.cma.2014.02.006
62. Shim KW, Monaghan DJ, Armstrong CG. Mixed dimensional coupling in finite element stress analysis. *Eng Comput*. 2002;18(3):241–252. doi:10.1007/s003660200021
63. Yamamoto T, Yamada T, Matsui K. Numerical procedure to couple shell to solid elements by using Nitsche's method. *Comput Mech*. 2019;63(1):69–98. doi:10.1007/s00466-018-1585-6

64. Turello DF. A variational approach to embed 1D beam models into 3D solid continua. *Comput Struct*. 2018;206:145-168.

65. Kerfriden P, Claus S, Mihai I. A mixed-dimensional CutFEM methodology for the simulation of fibre-reinforced composites. *Adv Model Simul Eng Sci*. 2020;7(1):18. doi:10.1186/s40323-020-00154-5

66. Lé B, Legrain G, Moës N. Mixed dimensional modeling of reinforced structures. *Finite Elem Anal Des*. 2017;128:1-18. doi:10.1016/j.finela.2017.01.002

67. Bourdin B, Francfort GA, Marigo JJ. The variational approach to fracture. *J Elast*. 2008;91(1-3):5-148. doi:10.1007/s10659-007-9107-3

68. Amor H, Marigo JJ, Maurini C. Regularized formulation of the variational brittle fracture with unilateral contact: numerical experiments. *J Mech Phys Solids*. 2009;57:1209-1229. doi:10.1016/j.jmps.2009.04.011

69. Miehe C, Welschinger F, Hofacker M. Thermodynamically consistent phase-field models of fracture: variational principles and multi-field FE implementations. *Int J Numer Methods Eng*. 2010;83(10):1273-1311. doi:10.1002/nme.2861

70. Borden MJ. *Isogeometric Analysis of Phase-Field Models for Dynamic Brittle and Ductile Fracture*. PhD thesis. University of Texas at Austin, Austin; 2012.

71. Hennig P. *Adaptive Isogeometric Analysis of Phase-Field Models*. PhD thesis. Dresden: Technische Universität Dresden; 2020. <https://nbn-resolving.org/urn:nbn:de:bsz:14-qucosa2-738116>.

How to cite this article: Ambati M, Heinzmann J, Seiler M, Kästner M. Phase-field modeling of brittle fracture along the thickness direction of plates and shells. *Int J Numer Methods Eng*. 2022;123(17):4094-4118. doi: 10.1002/nme.7001

APPENDIX A. EQUILIBRIUM OF PARTLY BROKEN STRUCTURES

As already mentioned in the discussion of the simply supported beam, the results of the mixed-dimensional model show that the partly broken shell features membrane action and membrane stress resultants despite of the load case comprising pure bending which, at first glance, is contradictory. It is in the following that this is actually necessary to establish an equilibrium state in the structure: This is done with an one-dimensional (1D) beam subjected to a line load \bar{p} similar to the one shown in the first numerical example, see Figure A1: this 1D beam shall be partly broken with the crack ranging from the bottom to exactly the middle of the thickness, that is, $a = t/2$. Furthermore, the crack shall be exactly in line with the thickness direction of the beam to simplify the deliberations. For the analytical proof, on the one hand, the cutting forces at the position $x = l_1/2$ are computed by establishing an equilibrium between them and the external loads and bearing forces (as illustrated in Figure A1). On the other hand, the definitions of the BERNOULLI beam theory (to which the KL shell theory reduces in this case) are used to condense the stresses in the beam cross section C to the same cutting forces

$$F_N = \int_C \sigma_{xx} dC = l_2 \int_t \sigma_{xx} dz \stackrel{!}{=} 0, \tag{A1a}$$

$$F_T = \int_C \sigma_{xz} dC = l_2 \int_t \sigma_{xz} dz \stackrel{!}{=} F_A - \bar{p} \frac{l_1}{2} = 0, \tag{A1b}$$

$$M_B = \underbrace{\int_C \sigma_{xx} dC}_{\text{from BERNOULLI beam theory}} = l_2 \underbrace{\int_t \sigma_{xx} z dz}_{\text{from equilibrium}} \stackrel{!}{=} F_A \frac{l_1}{2} - \bar{p} \frac{l_1}{2} \frac{l_1}{4} = \bar{p} \frac{l_1^2}{8}. \tag{A1c}$$

Next, the previously described ansatz for the here relevant stress components is adopted for the 1D beam

$$\sigma_{xx} = \sigma^m + z\sigma^b, \tag{A2a}$$

$$\sigma_{xz} = 0, \tag{A2b}$$

entailing a constant membrane part σ^m and a linear bending part σ^b over the height. To ease the evaluation of the equations, the phase-field over the thickness is simplified by substituting the continuous distribution with a HEAVISIDE step function as also shown in Figure A1. The phase-field is again coupled to the displacement field with the degradation

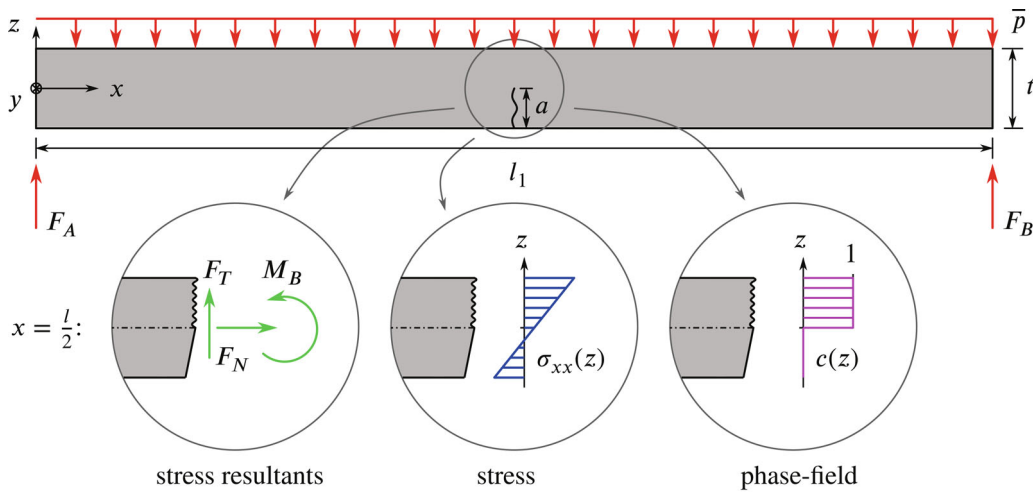


FIGURE A1 Partly broken beam with stress resultants, stresses, and the phase-field

function. By comparing the stress resultants as computed with the beam theory incorporating the stress ansatz to the ones obtained from the equilibrium

$$0 = l_2 \int_{-t/2}^0 \underbrace{g[c(z)]}_{=0} \sigma_{xx}(z) dz + l_2 \int_0^{t/2} \underbrace{g[c(z)]}_{=1} \sigma_{xx}(z) dz, \quad (\text{A3a})$$

$$\frac{\bar{p}}{l_2} \frac{l_1^2}{8} = \int_{-t/2}^0 \underbrace{g[c(z)]}_{=0} \sigma_{xx}(z) z dz + \int_0^{t/2} \underbrace{g[c(z)]}_{=1} \sigma_{xx}(z) z dz, \quad (\text{A3b})$$

and solving the arising equation system,

$$\sigma^m = \frac{12l_1^2 \bar{p}}{l_2 t^3}, \quad (\text{A4a})$$

$$\sigma^b = -\frac{3l_1^2 \bar{p}}{l_2 t^2} = -\frac{t}{4} \sigma^m, \quad (\text{A4b})$$

can be found. The resulting $\sigma^m \neq 0$ in fact shows that membrane action is necessary to establish an equilibrium state in a partly broken structural part, as it was stated at the beginning of this proof. Thereby, this phenomenon ultimately also renders the individual parts of the strain and stress to not be directly interpretable in the sense of membrane and bending action any more. The same circumstances to achieve equilibrium in a partly over the thickness broken beam is not limited to this special case but holds true for more complex loading cases and geometries as well.